AD-A278 379

REPORT DOCUMENTATION PAGE

1a. REPORT SECURITY CLASSIFICATION	1b. RESTRICTIVE MARKINGS
Unclassified	

2a. SECURITY CLASSIFICATION AUTHORITY

2b. DECLASSIFICATION / DOWNGRADING SCHEDULE

DTIC ELECTE APR 21 1994 S B D

3. DISTRIBUTION / AVAILABILITY OF REPORT

Unlimited Approved for public release, distribution unlimited

4. PERFORMING ORGANIZATION REPORT NUMBER(S)

UILU-ENG-94-4001

5. MONITORING ORGANIZATION REPORT NUMBER(S)

AFOSR-TR- 94 0163

6a. NAME OF PERFORMING ORGANIZATION	6b. OFFICE SYMBOL (If applicable)	7a. NAME OF MONITORING ORGANIZATION
The Board of Trustees of the University of Illinois		AFOSR/NA AFOSR/NA Bolling AFB DC 20332-6448

6c. ADDRESS (City, State, and ZIP Code)	7b. ADDRESS (City, State, and ZIP Code)
801 South Wright Street Champaign, IL 61820	Building 410 Bolling AFB, DC 20332-6448

8a. NAME OF FUNDING / SPONSORING ORGANIZATION	8b. OFFICE SYMBOL (If applicable)	9. PROCUREMENT INSTRUMENT IDENTIFICATION NUMBER
AFOSR/NA	NA	AFOSR-90-0156

8c. ADDRESS (City, State, and ZIP Code)

AFOSR/NA
Bolling AFB DC 20332-6448

10. SOURCE OF FUNDING NUMBERS

PROGRAM ELEMENT NO.	PROJECT NO.	TASK NO.	WORK UNIT ACCESSION NO.
61102F	2307	BS	

11. TITLE (Include Security Classification)

Real-Time Adaptive control of Mixing in a Plane Shear Layer

12. PERSONAL AUTHOR(S)

Arne J. Pearlstein

13a. TYPE OF REPORT	13b. TIME COVERED	14. DATE OF REPORT (Year, Month, Day)	15. PAGE COUNT
Final	FROM 900115 TO 930714	94,02,02	64

16. SUPPLEMENTARY NOTATION

17. COSATI CODES

FIELD	GROUP	SUB-GROUP

18. SUBJECT TERMS (Continue on reverse if necessary and identify by block number)

19. ABSTRACT (Continue on reverse if necessary and identify by block number)

Work was conducted on two projects related to real-time control of shear flows. In the first, two-dimensional unsteady simulations of the development of the wake behind a circular cylinder impulsively started into rotatory and rectilinear motion were performed. This simulation code is now serving as a testbed for the development of open- and closed-loop strategies for control of the lift/drag ratio as well as the suppression of vortex shedding. The code has been checked by comparison to earlier computational and experimental work. In the second project, a technique was developed to extract both velocity components in a two-dimensional incompressible flow from measurements of a single scalar (temperature or concentration), and all three velocity components in a three-dimensional incompressible flow from measurements of two scalars. The technique is applicable to steady or unsteady, laminar or turbulent flows. A key advantage over particle image velocimetry and other multi-point techniques is that our method uses full-field optical measurements, so that spatial resolution is not limited by particle size and loading restrictions.

20. DISTRIBUTION / AVAILABILITY OF ABSTRACT	21. ABSTRACT SECURITY CLASSIFICATION
☐ UNCLASSIFIED/UNLIMITED ☒ SAME AS RPT. ☐ DTIC USERS	UNCLASSIFIED

22a. NAME OF RESPONSIBLE INDIVIDUAL	22b. TELEPHONE (Include Area Code)	22c. OFFICE SYMBOL
DR. JAMES McMICHAEL	202-767-4936	NA

DD Form 1473, JUN 86   Previous editions are obsolete.   SECURITY CLASSIFICATION OF THIS PAGE

Real-Time Adaptive Control of Mixing in a Plane Shear Layer

Arne J. Pearlstein
Department of Mechancial and Industrial Engineering
University of Illinois at Urbana-Champaign
1206 west Green Street
Urbana, IL   61801

February 2, 1994

Final report on AFOSR Grant 90-0156

94-12127

94 4 20 051

Technical Report on AFOSR Grant 90-0156
Real-Time Adaptive Control of Mixing in a Plane Shear Layer

Arne J. Pearlstein, Principal Investigator

Department of Mechanical and Industrial Engineering

University of Illinois at Urbana-Champaign

1206 West Green Street

Urbana, IL 61801

Summary

Work was conducted on two projects related to real-time control of shear flows. In the first, two-dimensional unsteady simulations of the development of the wake behind a circular cylinder impulsively started into rotatory and rectilinear motion were performed. This simulation code is now serving as a testbed for the development of open- and closed-loop strategies for control of the lift/drag ratio as well as the suppression of vortex shedding. The code has been checked by comparison to earlier computational and experimental work. In the second project, a technique was developed to extract both velocity components in a two-dimensional incompressible flow from measurements of a single scalar (temperature or concentration), and all three velocity components in a three-dimensional incompressible flow from measurements of two scalars. The technique is applicable to steady or unsteady, laminar or turbulent flows. A key advantage over particle image velocimetry and other multi-point techniques is that our method uses full-field optical measurements, so that spatial resolution is not limited by particle size and loading restrictions.

1. Development of the Wake behind a Circular Cylinder Impulsively Started into Rotatory and Translational Motion

We (Chen, Ou & Pearlstein 1993) have completed a computational study of the temporal development of two-dimensional incompressible flow generated by a circular cylinder impulsively started into steady rotatory and rectilinear motion at Re = 200 (based on the cylinder diameter 2a and the magnitude U of the rectilinear velocity). We have used an explicit finite-difference/pseudo-spectral technique and a new implementation of the Biot-Savart law to integrate a velocity/vorticity formulation of the Navier-Stokes equations. Results are presented for the four angular/rectilinear speed ratios $\alpha = \Omega a/U$ (where W is the angular speed) considered experimentally by Coutanceau & Ménard (1985). For $\alpha \leq 1$, extension of

the computations to larger dimensionless times than possible in the work of Coutanceau & Ménard or considered computationally by Badr & Dennis (1985) allows for a more complete discussion of the long-time development of the wake. We discuss several aspects of the vortex kinematics and dynamics not revealed by the earlier work, in which vortex cores were identified from frame-dependent streamline and streamfunction information, rather than from the frame invariant vorticity distribution, as in the present work. Our results indicate that at Re = 200, vortex shedding does indeed occur for α = 3.25 (and possibly for larger α), in contrast to the conclusion of Coutanceau & Ménard. Moreover, the shedding process is very different from that associated with the usual Kármán vortex street for α = 0. Specifically, consecutive vortices can be shed from one side of the cylinder and be of the same sense, in contrast to the nonrotating case, in which mirror-image vortices of opposite sense are shed alternately from opposite sides of the cylinder.

The code is now being used in the development of open- and closed loop strategies for controlling the lift/drag ratio (Ou & Burns) and suppressing vortex shedding (Tsai, Bentsman & Pearlstein). A copy of a paper published in *J. Fluid Mech.* is included as Appendix A, and a reprint is enclosed.

2. Determination of Two- and Three-Dimensional Incompressible Velocity Fields from Measurements of Passive or Reactive Scalars

We have developed a technique for determining the velocity fields in two- and three-dimensional incompressible flows from full-field measurements of one or two passive or reactive scalars. Our technique is based on the recognition that if the transport equation(s) for the scalar(s) is (are) linear, then it (they) and the incompressible continuity equation

$$\nabla \cdot u = 0 , \qquad\qquad (1)$$

constitute two (three) linear equations in two (three) unknown velocity components. The method is fully described in Appendix B, which is a preprint of a manuscript submitted to *Physics of Fluids.*

In n dimensions, we reduce (1) and n- scalar transport equations to n uncoupled linear hyperbolic equations in the n velocity components. Given the scalar field data, solution of this systems is made unique by specification of appropriate boundary conditions. Boundary values of the unknown velocity components, rather than the scalars are required. We note that only spatial derivatives of the velocity components appear in these equations. Thus no initial data on the velocity field are required. A desirable consequence of the fact that the hyperbolic

2

equations are not initial value problems is that errors in the determination of the velocity field do not grow in time.

In two dimensions, the equations are singular at any point at which the gradient of the scalar vanishes, and in three dimensions they are singular at points for which one or more components of the cross product of the gradients of the scalars vanish. We have shown that these singularities are completely removable (in the sense that the extracted velocity field is smooth and can be uniquely determined) unless the gradient of the scalar vanishes identically over an area (in two dimensions) or the cross product of the gradients of the scalars vanishes identically over a volume (in three dimensions). In that case, the scalar field does not provide enough information to determine the velocity field, and any method necessarily fails.

We have also analyzed three methods which claim to extract the velocity field (for incompressible or compressible flows) from measurements of a single scalar. For one, the "iterative inversion" technique (Dahm et al. 1992), it is shown that if convergence does occur, then that result must be a consequence of spatial discretization, since in the limit of "full" resolution, it can be proved that the proposed iteration cannot converge. For the second, "variational" technique of Tokumaru & Dimotakis (1994) which seeks the "smoothest" velocity field, we point out that although the correct flow is not always the smoothest one consistent with the transport data, there are likely to be situations in which the correct velocity field and the smoothest velocity field do not differ by very much. Finally, we show that, for a second "variational" technique, the criteria imposed on the velocity field are not satisfied unless either the flow is steady and inertial terms are negligible, or the viscous terms can be written as the gradient of a scalar potential. Neither of these situations is likely to obtain in flows of interest.

Finally, we have completed a two-dimensional proof-of-concept study (Carpenter 1993) showing that the velocity field can be extracted from a computed scalar in a diverging channel flow. The extracted velocity field is nonparallel, and fully two-dimensional. The results clearly show that the solenoidal velocity field can be extracted from a single scalar in two dimensions. A detailed study of the effects of noise and spatial resolution is underway.

Joint work with Professor Ari Glezer is underway to implement this method in the plane mixing layer facility at Georgia Tech, with an eye toward real-time sensing and control.

References

Badr, H.M. & Dennis, S.C.R. *J. Fluid Mech.* **158**, 447-488 (1985).

Carpenter, B.N. M.S. Thesis, University of Illinois at Urbana-Champaign (1993).

Chen, Y.M., Ou, Y.R. & Pearlstein, A.J. *J. Fluid Mech.*, **253**, 449-484 (1993).

Coutanceau, M. & Ménard, C. *J. Fluid Mech.* **158**, 399-446 (1985).

Dahm, W.J.A., Su, L.K. & Southerland, K.B. *Phys. Fluids A* **4**, 2191-2206 (1992).

Tokumaru, P.T. & Dimotakis, P.E. *Expts. in Fluids*, accepted for publication (1994).

Appendix   A

449

Development of the wake behind a circular cylinder impulsively started into rotatory and rectilinear motion

By YEN-MING CHEN[1]†, YUH-ROUNG OU[2]‡
AND ARNE J. PEARLSTEIN[3]

[1] NASA-Langley Research Center, Hampton, VA 23665, USA

[2] Institute for Computer Applications in Science and Engineering, NASA-Langley Research Center, Hampton, VA 23665, USA

[3] Department of Mechanical and Industrial Engineering, University of Illinois at Urbana-Champaign, 1206 West Green Street, Urbana, IL 61801, USA

The temporal development of two-dimensional viscous incompressible flow generated by a circular cylinder impulsively started into steady rotatory and rectilinear motion at $Re = 200$ (based on the cylinder diameter $2a$ and the magnitude U of the rectilinear velocity) is studied computationally. We use an explicit finite-difference/pseudospectral technique and a new implementation of the Biot–Savart law to integrate a velocity/vorticity formulation of the Navier–Stokes equations. Results are presented for the four angular:rectilinear speed ratios $\alpha = \Omega a/U$ (where Ω is the angular speed) considered experimentally by Coutanceau & Ménard (1985). For $\alpha \leqslant 1$, extension of the computations to dimensionless times larger than achieved either in the experimental work or in the computations of Badr & Dennis (1985) allows for a more complete discussion of the temporal development of the wake. Using the frame-invariant vorticity distribution, we discuss several aspects of the vortex kinematics and dynamics not revealed by the earlier work, in which vortex cores were identified from frame-dependent streamline and streamfunction information. Consideration of the flow in the absence of sidewalls confirms the artifactual nature of the trajectory of the first vortex reported by Coutanceau & Ménard for $\alpha = 3.25$. For α greater than unity (the largest value considered by Badr & Dennis), our results indicate that at $Re = 200$ shedding of more than one vortex does indeed occur for $\alpha = 3.25$ (and possibly for larger α), in contrast to the conclusion of Coutanceau & Ménard. Moreover, the shedding process is very different from that associated with the usual Kármán vortex street for $\alpha = 0$. Specifically, consecutive vortices can be shed from one side of the cylinder and be of the same sense, in contrast to the non-rotating case, in which mirror-image vortices of opposite sense are shed alternately from opposite sides of the cylinder. The results are discussed in relation to the possibility of suppressing vortex shedding by open- or closed-loop control of the rotation rate.

† Present Address: General Electric Aircraft Engines, 1 Neumann Way, Cincinnati, OH 45215, USA.

‡ Present Address: Interdisciplinary Center for Applied Mathematics, Virginia Polytechnic Institute and State University, Blacksburg, VA 24061, USA.

1. Introduction

Flow past a rotating circular cylinder is a prototypical problem in the study of unsteady flow separation (Telionis 1981). It is also of considerable practical importance in boundary-layer control on airfoils (cf. Tennant, Johnson & Krothapalli 1976 and Modi, Mokhtarian & Yokomizo 1990), and in lift enhancement schemes employing the Magnus effect (Swanson 1961). Rotation of all or part of a body may also have applications in active or feedback control of vortex shedding, with important consequences for wake modification and the reduction of flow-induced vibration.

In this work, we describe the development of the two-dimensional flow generated by a circular cylinder of radius a started impulsively into combined steady rotatory and rectilinear motion, with angular speed Ω about its axis and rectilinear speed U normal to its generators. The fluid is taken to be at rest initially. The two parameters governing the development of the flow are the Reynolds number, defined by $Re = 2aU/v$, where v is the kinematic viscosity, and the ratio of rotatory to rectilinear speeds, defined by $\alpha = \Omega a/U$.

Experimental studies of the nominally two-dimensional flow past a circular cylinder undergoing steady rotatory and rectilinear motion have been conducted by Prandtl (Prandtl 1925; Prandtl & Tietjens 1934), Taneda (1977, 1980), Koromilas & Telionis (1980), Díaz *et al.* (1983), Werlé (1984), and Kimura, Tsutahara & Wang (1992). The most detailed work is that of Coustanceau & Ménard (1985) and Badr *et al.* (1990), in which papers an excellent summary of earlier work can be found. On the basis of their experiments (primarily at $Re = 200$, but including results for Re as high as 1000), Coutanceau & Ménard (1985) concluded that a (modified) Kármán vortex street

> disappears completely for α greater than a certain limiting value α_L. The value of α_L has been found to be not very dependent on the Reynolds number and to be about 2. For $\alpha > \alpha_L$ no other eddy is created after E_1 (the first eddy formed) during the time of the observations, so that the eddy street must have been destroyed.

They found this conclusion to be consistent with the earlier experimental work at higher Re by Prandtl, Díaz *et al.*, and Werlé and proposed, as a simple physical explanation for the disappearance of the Kármán vortex street at sufficiently high values of α, that

> for low values of α, eddies would be alternately shed on each side of the cylinder to form a Bénard–Kármán street, as for the pure translation ($\alpha = 0$). But the eddies on the side moving in the direction of the rotation decrease progressively when α increases and then disappear completely. Thus it was found that the Bénard–Kármán structure begins to deteriorate as soon as the peripheral velocity becomes greater than the free-stream velocity (giving rise to a zigzag oscillating wake) and finally disappears for $\alpha > 2.5$.

When one examines the evidence for these statements, one finds that it is not overwhelmingly strong at lower values of Re, particularly for the critical value of α and its dependence on Re. For $Re = 9000$ and several values of α, Díaz *et al.* (1983) made hot-wire measurements of the streamwise velocity, and computed its autocorrelation. They found that for $\alpha = 0$ and 1, the velocity autocorrelations were very similar, approximately periodic, and had local maxima separated by a time corresponding to the nominal Strouhal frequency. For $\alpha = 1.5$ and 2, the autocorrelation function was progressively reduced. Díaz *et al.* (1983) did indeed conclude that 'for peripheral velocities up to the value of the free-stream velocity, a distinct Kármán vortex activity exists within the wake, whereas for greater peripheral velocities, the Kármán activity deteriorates and disappears for values in excess of twice the free-stream velocity.' On

the other hand, for $Re \approx 3300$ Werlé (1984) noted that for values of α in excess of that at which separation is eliminated, 'when the tangential velocity increases further, the cylinder finally entrains an entire layer of relatively turbulent fluid in its rotation. More or less periodic instabilities then appear.' From this, it is not clear whether vortex shedding is really suppressed by rotation at $Re \approx 3300$. At $Re = 10^3$, Badr *et al.* (1990) found experimentally and computationally that the second vortex was formed much later for $\alpha = 2$ than for $\alpha = 1$, and was also much weaker. For $\alpha = 3$, their experiments and computations showed that the first two vortices formed were of the same rotational sense, and that one of the vortices is shed downstream, while the other 'is washed down to the frontal part of the cylinder and disappears'. For larger dimensionless times, their two-dimensional computations show that no additional vortices are formed, and the computed flow approaches a steady state. In their experiments, 'three-dimensional and instability effects become more pronounced, especially in the wake'. At the lower Re in the experiments of Coutanceau & Ménard (1985), the towing tank used allowed observations to be made over only a very limited range of dimensionless time.

The issues of whether the Kármán vortex street is destroyed and vortex shedding is suppressed are of considerable practical interest from the standpoint of wake modification and the reduction of flow-induced vibration. In particular, it is of interest to determine whether, for a given Re, there is a value of α_L beyond which (two- or three-dimensional) vortex shedding disappears. An additional factor tending to complicate the experimental resolution of these issues is that in either a fixed reference frame or one translating with the cylinder, the generation and shedding of vortices is easily masked (Perry, Chong & Lim 1982) at large values of α by the high velocities induced in the near wake by the rapidly rotating cylinder. Although experimental techniques for measuring vorticity are under development for two- and three-dimensional flows (cf. Klewicki & Falco 1991), the vorticity distribution frequently can be determined conveniently by direct computation of the vorticity, which is a frame-invariant quantity.

To date, however, most of the theoretical studies have shed no light on the question of whether cylinder rotation can suppress vortex shedding. The analytical investigations of flow past a rotating and translating circular cylinder (Krahn 1955; Glauert 1957*a*, *b*; Moore 1957; and Wood 1957) are based on steady boundary-layer theory, and are hence inapplicable to investigation of the unsteady separated flow associated with vortex shedding. The computational investigations of flow generated by a rotating and translating cylinder reported by Ta Phuoc Loc (1975), Lyulka (1977), Townsend (1980), Ingham (1983), Ingham & Tang (1990), and Tang & Ingham (1991) concern only the steady flow with $Re \leqslant 30$. Although Shkadova (1982) discussed a computational algorithm for the unsteady flow, she presented only a single set of streamlines for each of a few combinations of Re and α ($Re = 20$, 40, and 80 for $\alpha = 0.2$, and $Re = 40$ for $\alpha = 3$). She did not discuss unsteady effects for the case of a rotating and translating cylinder, and it is not clear whether the streamlines presented for each combination of Re and α pertained to a computed steady flow, or to instantaneous streamlines (at unspecified times) in an unsteady flow. In the earlier work of Simuni (1967) concerning the flow generated by a cylinder accelerated smoothly (rather than impulsively) into rotatory and rectilinear motion, the time-dependence of the body motion was not clearly specified, nor was any information provided about the time-dependence of the computed solution.

To the best of our knowledge, other than the experimental work of Coutanceau & Ménard (1985), Badr *et al.* (1990), and Kimura *et al.* (1992), the only investigations of

vortex shedding by a steadily rotating and translating circular cylinder in the laminar regime are the computational studies of Badr & Dennis (1985), Badr, Dennis & Young (1989), Badr *et al.* (1990), Kimura *et al.* (1992) and Chang & Chern (1992). Although Badr and coworkers realized the importance of extending the computations to larger α, their work for $Re = 200$ was limited to $\alpha \leqslant 1$, and so shed no light on the conclusion of Coutanceau & Ménard (1985) cited above. The computational work of Kimura *et al.*, covering the Re range from approximately 400 to 10^4, uses a discrete vortex method with the cylinder surface divided into only 14 segments. The smallest Re at which these authors present results is at a poorly defined value near 400, for which they indicate only that 'meandering' of the wake occurs for $\alpha \leqslant 1.8$, and that for $\alpha \geqslant 2.6$ 'meandering disappears, but this value is not so definitive'. On the other hand, although the extensive and well-resolved two-dimensional computations of Chang & Chern support the authors' detailed description of different two-dimensional flow regimes in the range $10^3 \leqslant Re \leqslant 10^6$, $\alpha \leqslant 2$, they concern a range of Re and α in which, on the basis of what is known of the non-rotating case (Williamson 1988), the two-dimensionality of the flow is in doubt.

In the present work, for $Re = 200$, we present computations extending the range of α to the highest value (3.25) studied experimentally by Coutanceau & Ménard (1985). After comparing our results at lower values of α to the previous work of Coutanceau & Ménard (1985) and Badr & Dennis (1985), we present results for the two largest values of α (2.07 and 3.25) considered by the former authors. Ours is the first computational investigation at $Re = 200$ for $\alpha > 1$, and is significant in the light of the earlier conclusions that vortex shedding is suppressed for $\alpha > 1$ or $\alpha > 2.5$. Our computed results are in excellent agreement with the experiments of Coutanceau & Ménard (1985) for $Re = 200$ and $\alpha = 2.07$. We then present strong evidence in support of the hypothesis that rotation does not suppress vortex shedding for $Re = 200$ and $\alpha = 3.25$. This evidence, consisting of streamlines viewed from a reference frame moving with a vortex, and of contours of constant vorticity, is of a type not easily obtainable in the laboratory, and provides an important demonstration of the capability of computational methods to resolve questions arising from experiment.

In §2, we present the governing equations, along with a transformed version appropriate for computations with a body-fitted time-dependent grid used for $\alpha = 3.25$. In §3, we briefly describe the numerical methods employed, including a new implementation of the Biot–Savart law used to satisfy boundary conditions on the vorticity at the cylinder and on the velocity in the far field. Section 4 discusses a technique, more general than that employed in earlier studies, for determining the initial flow (at $t = 0^+$). The main results, inluding comparison to the experiments of Coutanceau & Ménard (1985) and discussion of features of the flow not elucidated by their work or earlier computations, are presented in §5, followed by a more general discussion in §6.

2. Governing equations

A non-rotating reference frame translating with the cylinder is used in this study. In this frame, the fluid at infinity has a uniform velocity of magnitude U in the x-direction, and the cylinder rotates in the counterclockwise direction with angular velocity Ωe_z, as shown in figure 1.

We use a velocity/vorticity formulation, consisting of the vorticity transport
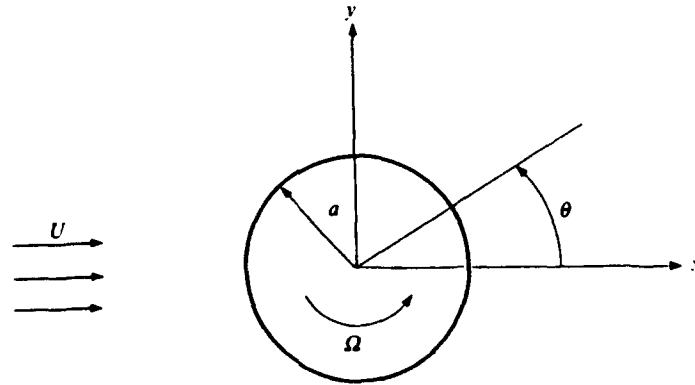
FIGURE 1. Definition sketch.

equation and a vector Poisson equation for velocity. In two dimensions, the dimensionless equations are (Wu 1975; Fasel 1976):

$$\frac{\partial \omega}{\partial t} + V \cdot \nabla \omega = \frac{2}{Re} \nabla^2 \omega, \tag{1}$$

and

$$\nabla^2 V = -\nabla \times (\omega e_z), \tag{2}$$

where we use the cylinder radius a as the lengthscale, and a/U as the timescale. The velocity is normalized by U. Equation (2) is derived from the continuity equation

$$\nabla \cdot V = 0, \tag{3}$$

the definition of vorticity for a two-dimensional flow

$$\omega e_z = \nabla \times V, \tag{4}$$

and the vector identity

$$\nabla \times \nabla \times V = \nabla(\nabla \cdot V) - \nabla^2 V, \tag{5}$$

where $V = u e_x + v e_y$ is the velocity vector.

The dimensionless boundary conditions are

$$V = e_x \qquad \text{at infinity} \tag{6}$$

and

$$V = x(-e_x \sin \theta + e_y \cos \theta) \quad \text{on the cylinder surface.} \tag{7}$$

To allow for computation of the flow on a time-dependent grid, we write (1) and the components of (2) in general body-fitted (ξ, η)-coordinates as

$$\omega_t = \frac{1}{J}[x_t(\omega_\xi y_\eta - \omega_\eta y_\xi) - y_t(\omega_\xi x_\eta - \omega_\eta x_\xi) - y_\eta(u\omega)_\xi + y_\xi(u\omega)_\eta - x_\eta(v\omega)_\xi + x_\xi(v\omega)_\eta]$$

$$+ \frac{2}{ReJ^2}(\delta\omega_{\xi\xi} - 2\beta\omega_{\xi\eta} + \gamma\omega_{\eta\eta}) + \frac{2}{Re}(P\omega_\xi + Q\omega_\eta), \tag{8}$$

$$\delta u_{\xi\xi} - 2\beta u_{\xi\eta} + \gamma u_{\eta\eta} + J^2(Pu_\xi + Qu_\eta) = J(\omega_\xi x_\eta - \omega_\eta x_\xi), \tag{9}$$

and

$$\delta v_{\xi\xi} - 2\beta v_{\xi\eta} + \gamma v_{\eta\eta} + J^2(Pv_\xi + Qv_\eta) = J(\omega_\xi y_\eta - \omega_\eta y_\xi) \tag{10}$$

(Reddy & Thompson 1977) where

$$\delta = x_\eta^2 + y_\eta^2, \quad \beta = x_\eta x_\xi + y_\eta y_\xi, \quad \gamma = x_\xi^2 + y_\xi^2, \\ P = \xi_{xx} + \xi_{yy}, \quad Q = \eta_{xx} + \eta_{yy} \quad\quad\quad (11)$$

and

$$J = x_\xi y_\eta - x_\eta y_\xi \quad\quad\quad (12)$$

is the Jacobian of the mapping between the (x, y)- and (ξ, η)-coordinate systems. Here, subscripts denote partial differentiation. In (8) and in the computer code developed, we have allowed the grid in the physical (x, y)-space to be time-dependent. This introduces additional terms associated with x_t and y_t into the governing equations in the generalized coordinate system. In this work, the body-fitted grid is simply one of cylindrical polar coordinates and is time-independent, except for $\alpha = 3.25$ where the grid is made time-dependent for $24 \leqslant t \leqslant 54$. The grid is uniformly spaced in the circumferential direction and is stretched in the radial direction, as described below.

3. Numerical methods

In this and other numerical simulations, it is necessary to confine the computation to a finite spatial domain. As a result, (6) cannot be applied directly at the outer perimeter of the computational domain. Various far-field boundary conditions, including those derived from potential flow and Oseen expansions, have been adopted in the past. The conditions imposed at the outer perimeter of the computational domain have been found to strongly influence the accuracy of steady flow computations in this unbounded geometry (Fornberg 1980; Ingham 1983; Ingham & Tang 1990). A second difficulty, common to most simulations based on primitive variable (pressure/velocity) or velocity/vorticity formulations, is that conditions on either the pressure or vorticity are required at solid boundaries. In this work, both of these difficulties are resolved by use of a new implementation of the Biot–Savart law briefly described below. For further details, the reader is referred to the work of Wu and coworkers (Wu & Thompson 1973; Wu 1976; Wang & Wu 1986), and Chen (1989).

The definition (4) allows determination of the vorticity field from a known velocity field. Conversely, one can determine the velocity field from a known vorticity field via the generalized Biot–Savart law, which in two dimensions can be written as

$$V(r_0, t) = -\frac{1}{2\pi} \iint_D \frac{\omega(r, t) e_z \times (r - r_0)}{|r - r_0|^2} \, dA - \frac{1}{2\pi} \iint_B \frac{2\Omega(t) e_z \times (r - r_0)}{|r - r_0|^2} \, dA + V_\infty \quad (13)$$

(Payne 1958; Wu 1976), where the subscript 0 denotes the field point where the velocity is evaluated, and V_∞ is the uniform flow at infinity. The first double integral in (13) is evaluated numerically over the fluid domain D, while the second is evaluated analytically over the solid body B. Here, ωe_z is the vorticity at a point within the fluid, and Ωe_z is the angular velocity of a point within B.

Equation (13) serves two purposes in this study. First, if the vorticity field $\omega(r, t)$ is known and the domain D is large enough to contain all of the vorticity generated at the solid boundary prior to time t, then the velocity on the perimeter of D can be evaluated directly by numerical integration of (13). Second, by linking the velocity and vorticity fields, (13) provides a basis for determining the vorticity on the solid boundary. Applying (13) to points r_b on the solid boundary, one obtains

$$V(r_b, t) = -\frac{1}{2\pi} \iint_D \frac{\omega(r, t) e_z \times (r - r_b)}{|r - r_b|^2} \, dA - \frac{1}{2\pi} \iint_B \frac{2\Omega(t) e_z \times (r - r_b)}{|r - r_b|^2} \, dA + V_\infty. \quad (14)$$

f V_∞ and the body motion $V(r_b, t)$ and $\Omega(t)$ are given, and the vorticity is known everywhere except on the solid boundary, then the only unknown in (14) is the vorticity on the solid boundary. Therefore, one can solve (14) as a vector Fredholm integral equation of the first kind to obtain the vorticity values at grid points on the solid boundary.

In this work, the numerical integration of (13) and (14) is performed over each quadrilateral element in D using isoparametric representations commonly used in finite-element computations. All variables are located at the intersections of grid lines, namely corners of quadrilateral elements. The vorticity distribution over each quadrilateral element is approximated by bilinear shape functions. Integration is then performed over the $[-1, 1] \times [-1, 1]$ square in the isoparametric plane. When the field point is far from the quadrilateral element, more efficient asymptotic formulae (Weston & Liu 1982; Ting 1983) are employed. Further details are provided in Chen (1989).

In deriving the discretized forms of (8)–(10), second-order central differences are used for all derivatives in the radial direction η, while a pseudospectral transform method (Orszag 1980; Zang, Wong & Hussaini 1982) is used to evaluate all derivatives in the circumferential direction ξ. The cross-derivative terms are approximated by central differencing in η followed by pseudospectral transformtion in ξ. We use a fully explicit method to advance the vorticity transport equation (8) in time to obtain the vorticity values at the interior grid points. The vorticity on the outer perimeter of the computational domain is obtained by extrapolation. At this stage, the vorticity on the solid boundary lags by one time step. If this vorticity field were used to evaluate the right-hand side of (14), the result would not satisfy the no-slip and no-penetration conditions. The continuous generation of vorticity at the cylinder is properly simulated in our computations by adding or subtracting vorticity at the boundary at each time level in order to satisfy (14) identically.

It should be noted that the solution of (14) is not unique (Wu 1976; Taslim, Kinney & Paolino 1984). To render the solution unique, Wu (1976) developed and imposed the principle of vorticity conservation, which states that the total vorticity in the combined fluid and solid regions must be zero at all times. A more general and robust procedure. applicable to flows over single and multiple solid bodies, has been developed by Chen (1989), and is used here.

The computational loop to advance the solution from one time level to the next consists of the following steps:

(i) The discretized vorticity transport equation (8) is advanced explicitly to obtain new vorticity values at all interior grid points, using a second-order rational Runge–Kutta method (Wambecq 1978). In contrast to the three-step Adams–Bashforth method used by previous authors, this allows a much larger time-step size due to a less severe stability constraint.

(ii) Using known vorticity values at the interior grid points, the kinematic constraint (14) is used to update the vorticity values on the solid boundary.

(iii) Using the updated vorticity field. the velocity at points on the outer perimeter of the computational domain is evaluated from (13). Once velocity boundary values are known, Poisson equations (9) and (10) are solved for the new velocity field. The discretizations of (9) and (10) are 11-banded and block-diagonal in form. and are solved by a preconditioned biconjugate gradient algorithm (Chen, Koniges & Anderson 1989).

The method outlined above is particularly well-suited for the initial development of the flow generated by impulsively started bodies. This is so because the vorticity is initially concentrated near the solid body, thus allowing the numerical simulation to be

confined to a domain containing nearly all the vorticity. Since the velocity at the outer perimeter of the computational domain is *calculated* via (13), imposition of computational far-field velocity boundary conditions is avoided. The use of (13) in calculating the far-field velocity would be numerically exact at time t if the computational domain contained all the vorticity generated at the cylinder surface prior to t. We note that, in the streamfunction/vorticity formulation, the stream-function values on the outer perimeter of the computational domain can be obtained similarly by using an integral constraint equation (Wu & Sampath 1976). We also note that the velocity field can be obtained by applying (13) at every grid point. This results in a point-by-point scheme which, unlike schemes using the Poisson equations (9) and (10), does not require solution of large linear equation systems. This approach was adopted in Wu's earlier work, and might be attractive on massively parallel computers.

The size of the computational domain is chosen according to the time span investigated. Here, we set the outer boundary of the computational domain to be a circle of radius 24 for $t \leqslant 24$. For $\alpha = 3.25$, the grid is made time-dependent for $24 \leqslant t \leqslant 54$. We use 128 uniformly spaced and 120 stretched grid lines in the θ- and r-directions, respectively. The stretching function of Vinokur (1983) is used to distribute the circular grid lines on $1 \leqslant r \leqslant 24$. This stretching allows grid points to be clustered near one or both ends of the domain, or anywhere between, by adjusting two parameters s_0 and s_1. Here, s_0 and s_1 are the ratios of the spacing if N points were distributed uniformly, to the actual spacings at the inner and outer boundaries, respectively. For $\alpha = 0.5$ and 1.0, we set $s_0 = 5.0$ and $s_1 = 0.25$. The grid spacings adjacent to the cylinder and at the outer perimeter are 4% and 75% of the cylinder radius, respectively. For $\alpha = 2.07$ and 3.25, we set $s_0 = 10.0$ and $s_1 = 0.25$ to further cluster circular grid lines near the cylinder, with grid spacings adjacent to the cylinder and at the outer perimeter being 2% and 76% of the cylinder radius, respectively. At the end of the simulation, the vorticity magnitude on the outer perimeter is less than 10^{-5} for all cases except as noted, indicating that only a negligible fraction of the vorticity has escaped the domain.

With the grid chosen for $\alpha \leqslant 2.07$, our method requires approximately 5 CPU seconds per time step on a CRAY 2.

4. Determination of the initial flow

In most numerical simulations of flow over impulsively started bodies, the initial flow field is taken to be the potential flow, since the vorticity at $t = 0^+$ is concentrated on the body surface in the form of a vortex sheet. Perturbation solutions in which t is the small parameter have also been used as initial conditions (Collins & Dennis 1973 for $\alpha = 0$; Badr & Dennis 1985 for $\alpha \neq 0$). Both approaches require special techniques in order to obtain the initial flow field. In the present work, determination of the initial flow field requires no special treatment. The same procedure used for determining the boundary vorticity distribution satisfying the no-slip and no-penetration conditions is applied. More specifically, (14) is solved for the unknown boundary vorticity at $t = 0^+$, with the vorticity taken to be zero at every grid point away from the cylinder surface. Once the boundary vorticity values are obtained, the initial velocity field is determined by solving (9) and (10), with the velocity on the outer perimeter of the computational domain determined by application of (13) to points on the outer perimeter. This versatile procedure enables the numerical code to handle bodies of arbitrary shape undergoing arbitrary rotational and translational motion.

Errors in approximating the vorticity layer of infinitesimal thickness at $t = 0^-$ are inherent to any computational scheme. However, as discussed by Lugt & Haussling (1974), even in the worst case of a body set impulsively into motion, the duration of these errors is confined to a very limited time close to $t = 0$. For the present algorithm. this will be confirmed in §5 by comparison at small times of our numerical results to the perturbation solution of Badr & Dennis (1985).

5. Results

In this section, numerical results for $Re = 200$ with $\alpha = 0.5$, 1.0. 2.07, and 3.25 are presented and discussed. The parameter values chosen allow comparison to the experimental results of Coutanceau & Ménard (1985) and permit a critical evaluation of their conclusions regarding the suppression of vortex shedding by rotation.

For $\alpha = 0.5$ and 1.0, excellent agreement of our computed streamlines with previous experimental (Coutanceau & Ménard 1985) and numerical (Badr & Dennis 1985) results is obtained. For $\alpha = 2.07$, for which no numerical results have been reported previously, we obtain excellent agreement with experiment. For $\alpha = 3.25$, the relatively small disagreement between experiment and our computations is probably due to the effects of three-dimensionality and sidewall boundary layers in the former (see §5.4). For $\alpha = 0.5$, 1.0, and 2.07, we continue the simulations to larger dimensionless times ($t = 24$) than could be studied experimentally by Coutanceau & Ménard (1985), so that the nature of the wake development can be better discerned. For $\alpha = 3.25$, we extend our calculation to $t = 54$ to include shedding of the second and third vortices.

For the same values of α, we also present computations of the vorticity contours. which we find useful for studying vortex shedding without the effects of 'masking' associated with frame-dependent streamlines. We also present trajectories of the shed vortices, computed from vorticity contours and from streamlines.

We note that the timescale adopted here is the same as that used by Badr & Dennis (1985). Conversion of the dimensionless times of Coutanceau & Ménard (1985) to those herein requires multiplication of the former by a factor of two.

As discussed in §4, the solution procedure presented in §3 is applied at $t = 0^+$ to obtain the initial flow field. Errors are present due to the inability of any numerical scheme to resolve the infinitesimal vorticity layer at $t = 0^+$. To confine these errors to small times near $t = 0$, small initial time steps are used for all cases. For the first 20 time steps, $\Delta t = 10^{-4}$ is used. This is followed by 28 steps with $\Delta t = 10^{-3}$, which brings the time level in 0.03. A constant Δt (10^{-2} for $\alpha = 0.5$ and 1.0; 2.5×10^{-3} for $\alpha = 2.07$ and 3.25) is taken for the rest of each simulation. The time-step size is not dictated by the numerical stability constraint, but rather is chosen on the basis of accuracy considerations. To demonstrate the accuracy of the initial flow field, we show in figure $2(a-d)$ the variation of vorticity on the cylinder for four values of α at small times. The numerical results are compared to the asymptotic formula

$$\omega(1,\theta,t) \approx \frac{1}{\lambda}\left\{\alpha\left(\frac{2}{\pi^{\frac{1}{2}}}-\frac{\lambda}{2}\right)+\left(\frac{4}{\pi^{\frac{1}{2}}}+\lambda\right)\sin\theta+\left(2.7844\lambda-\frac{16}{3\pi^{\frac{1}{2}}}\right)\alpha t\cos\theta\right.$$

$$\left.+\left[6.5577\lambda-\frac{4}{\pi^{\frac{1}{2}}}\left(1+\frac{4}{3\pi}\right)\right]t\sin 2\theta\right\} \quad (15)$$

given by Badr & Dennis (1985), where

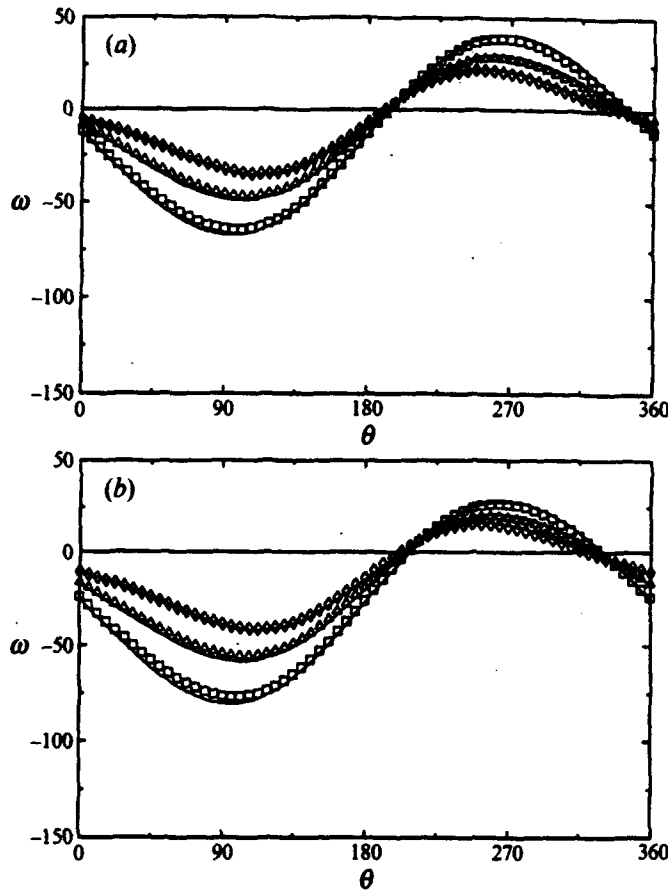$$\lambda = (8t/Re)^{\frac{1}{2}}. \quad (16)$$

FIGURE 2(*a, b*). For caption see facing page.

We see that agreement with the asymptotic results improves as *t* increases. Better agreement is achieved for $\alpha = 2.07$ and 3.25 than for smaller α since a smaller time-step size is used. These results demonstrate that errors are indeed confined to a very limited time close to $t = 0$, as reported by Lugt & Haussling (1974).

5.1. *Results for* $\alpha = 0.5$

In this subsection, we extend the $\alpha = 0.5$ computations of Badr & Dennis (1985) to larger dimensionless times than considered by them or in the experiments of Coutanceau & Ménard. The kinematics and dynamics of vortex shedding are discussed using instantaneous streamlines in two different reference frames, as well as vorticity distributions. The streamfunction is computed from the velocity field by a least-squares method described by Chen (1989).

Computations performed for $0 \leqslant t \leqslant 24$ show that the results are in excellent agreement with the experimental work of Coustanceau & Ménard (1985) for $1 \leqslant t \leqslant 13$ and the computations of Badr & Dennis (1985) for $1 \leqslant t \leqslant 12$. Figure 3(*a–j*) shows a sequence of instantaneous computed streamlines for $8 \leqslant t \leqslant 24$, viewed from a non-rotating frame translating with the circular cylinder. We adopt the notation used by Coutanceau & Ménard (1985) in their discussion of the flow
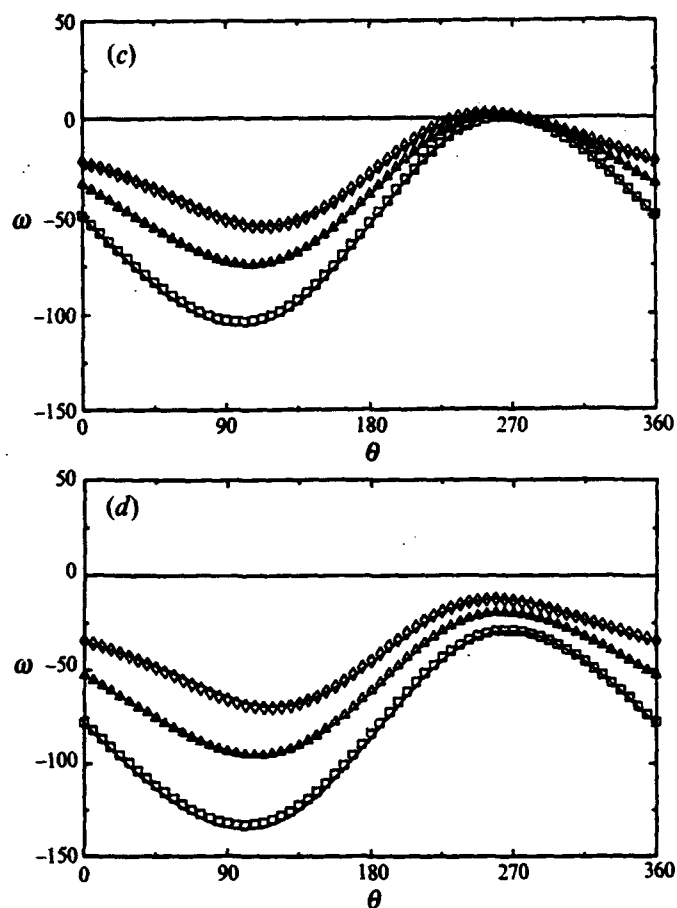
FIGURE 2. Evolution of the vorticity distribution on the surface of the cylinder at early times. $Re = 200$. Symbols: asymptotic solution; □, $t = 0.05$; △, $t = 0.1$; ◇, $t = 0.2$. ——, Numerical solution. (a) $\alpha = 0.5$, (b) $\alpha = 1.0$, (c) $\alpha = 2.07$, (d) $\alpha = 3.25$.

development for $t \leqslant 13$, to which the reader is referred. We observe that the coalescence of two 'intermediate' eddies E_3' and E_3'' to form eddy E_3 at $t \approx 12$ (figure $3c, d$) indeed repeats (at $t \approx 22$; figure $3h, i$) as predicted by Coutanceau & Ménard (1985). (The subscript here denotes the order of appearance of eddies after the impulsive start.) The transposition of saddle points S_2 and S_3' associated with eddies E_2 and E_3', respectively, discussed by Coutanceau & Ménard (1985) and sketched by Badr *et al.* (1986), is clearly shown in figure $3(a, b)$. Also, a common boundary for E_2 and E_3', which was difficult to observe experimentally (Coutanceau & Ménard 1985) due to limitations of the flow visualization technique, does indeed exist, as shown in figure $3(a)$. The common boundary soon becomes an 'alleyway' for fluid to pass through, as shown in figure $3(b)$. As noted by Eaton (1987), existence of such an alleyway in an unsteady flow does not imply that fluid is carried from one side of the wake to the other.

As discussed by Perry *et al.* (1982), the streamlines are not invariant with respect to a change in reference frame, and the vortex street can appear very differently in different frames. To best observe the development of a vortex, the observer should
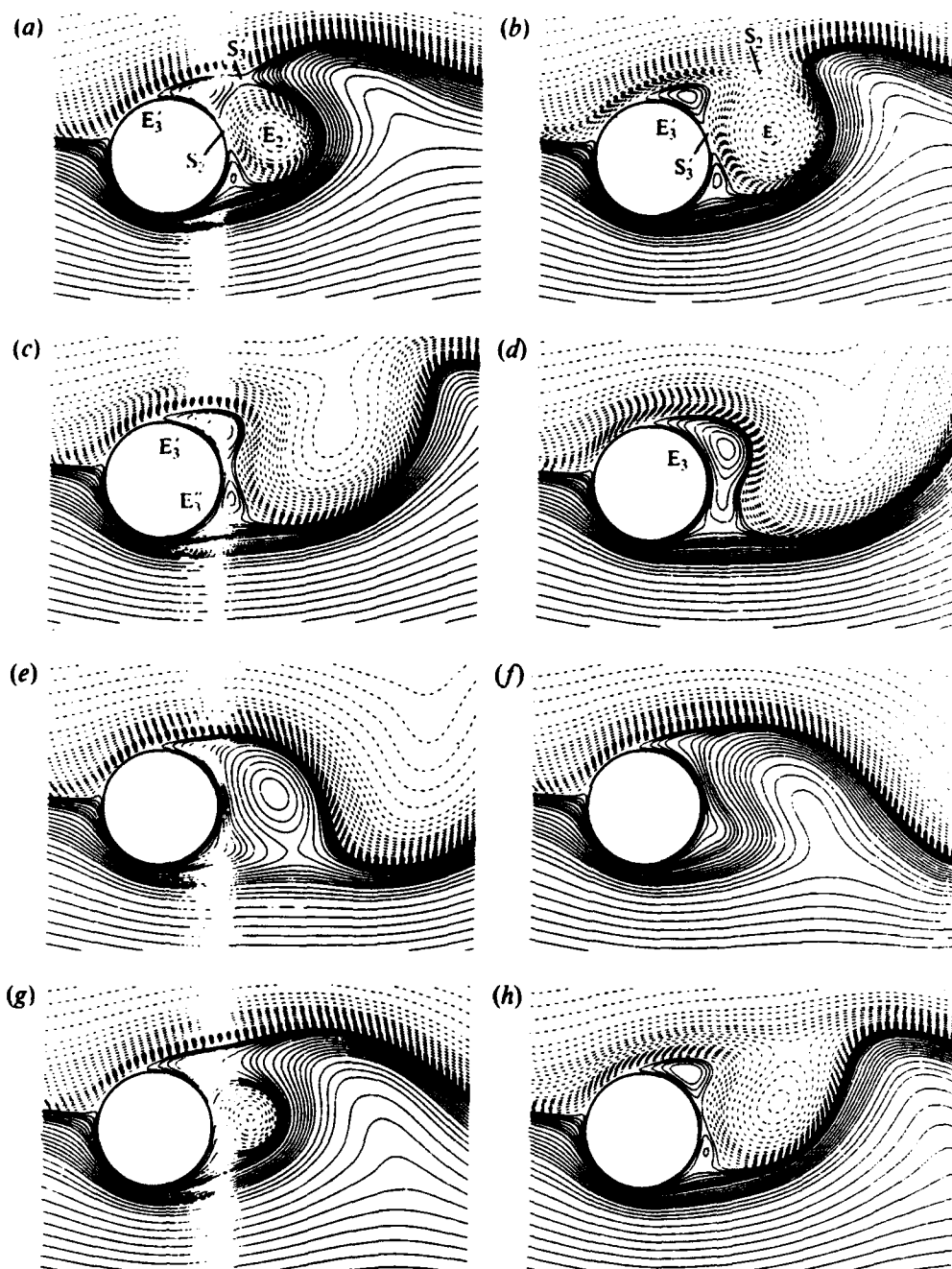
FIGURE 3(*a–h*). For caption see facing page.

move with its centre (Lugt 1979). Otherwise, the vortex can be masked by the motion of the observer relative to the vortex (Williamson 1985; Coutanceau & Ménard 1985). This masking phenomenon was described by Coutanceau & Ménard as the opening up of vortices and disappearance of closure points into a wave-like pattern, as sketched in Lugt (1979). Since an *attached* vortex translates with the cylinder, it can be clearly observed in a frame translating with the cylinder. However, after the vortex is shed, its
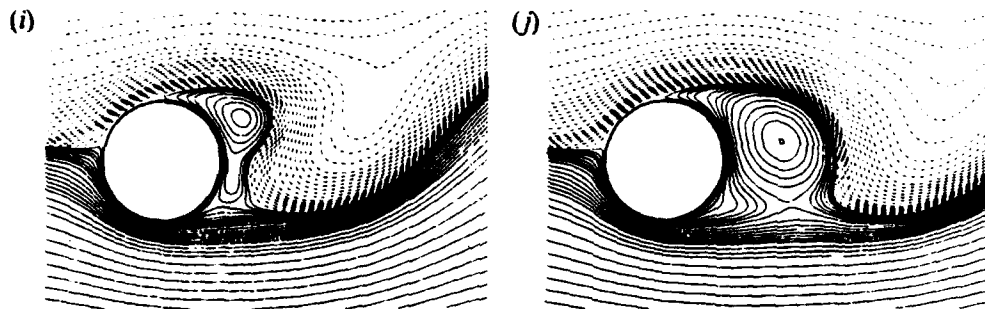
FIGURE 3. Instantaneous streamlines for $Re = 200$, $\alpha = 0.5$ at various times, viewed from a non-rotating frame translating with the cylinder. Streamlines with non-negative (including zero) and negative streamfunction values (ψ) are shown by solid and dashed lines, respectively. At each time, the cylinder is a streamline with $\psi = 0$. The values of ψ plotted are 0, -0.01, ± 0.02, -0.03, ± 0.04, ± 0.06, ± 0.08, ± 0.10, ± 0.12, ± 0.15, ± 0.20, ± 0.25, ± 0.30, ± 0.35, ± 0.40, ± 0.45, ± 0.50, ± 0.60, ± 0.70, ± 0.80, ± 1.00, with an increment of ± 0.2 thereafter. (a) $t = 8.0$, (b) 9.0, (c) 11.0, (d) 12.0, (e) 14.0, (f) 16.0, (g) 18.0, (h) 20.0, (i) 22.0, (j) 24.0.

core is, especially in the far wake, essentially stationary with respect to the free stream. Therefore, it is generally easier to observe *shed* vortices in a frame fixed with the undisturbed fluid. The instantaneous streamlines observed in such a frame are shown at selected times in figure 4(a–c). As expected, the shed vortices are clearly distinguishable. We note that two additional vortices are shed over an interval of about 10 dimensionless time units, and that the flow near the cylinder is very similar in figures 4(a) and 4(c). We further note that in a moving frame, the cylinder itself is not a streamline, and the attached vortices in figure 4(a–c) are now masked by the velocity field in the near wake of the cylinder. In a frame translating with the cylinder, however, the shed vortices are hidden in the oscillating wake, as shown in figure 5(a–c) for the values of t shown in figure 4(a–c).

At the same dimensionless times, figure 6(a–c) shows the corresponding vorticity contours, which are invariant with respect to translation of the observer. Because rotation divides the surface of the cylinder into 'downstream-moving' ($\pi < \theta < 2\pi$) and 'upstream-moving' ($0 < \theta < \pi$) parts, a basic symmetry of the vorticity field for the non-rotating ($\alpha = 0$) case (associated with the fact that for a T-periodic flow, the relations

$$u(r, \theta, t) = u(r, -\theta, t-\tau), \quad v(r, \theta, t) = -v(r, -\theta, t-\tau) \tag{17}$$

lead to $\omega(r, \theta, t) = -\omega(r, -\theta, t-\tau)$, where $0 < \tau < T$ is a phase difference) is broken. Nonetheless, the process is topologically similar to the $\alpha = 0$ case, with the shedding of vortices of alternating rotational sense being associated with the thinning and severance of elongated vorticity contours emanating from opposite sides of the cylinder. As in the experiments of Díaz *et al.* (1983) at higher Re, cylinder rotation has the effect of altering the initial trajectories of the shed vortices, although these are expected to become parallel to the direction of cylinder translation as the vortices move farther away from the rotating cylinder and are advected downstream. As in the $\alpha = 0$ case, vortices of opposite sense lie on opposite sides of a 'street', although the rotation has clearly displaced the midline of the street upward.

Figure 7(a, b) shows that the computation of vortex core and saddle trajectories using streamfunction values (in excellent agreement with the trajectories computed by Coutanceau & Ménard 1985 from experimental streamline data and shown in their figure 4a) can differ significantly from those computed using the vorticity distribution.
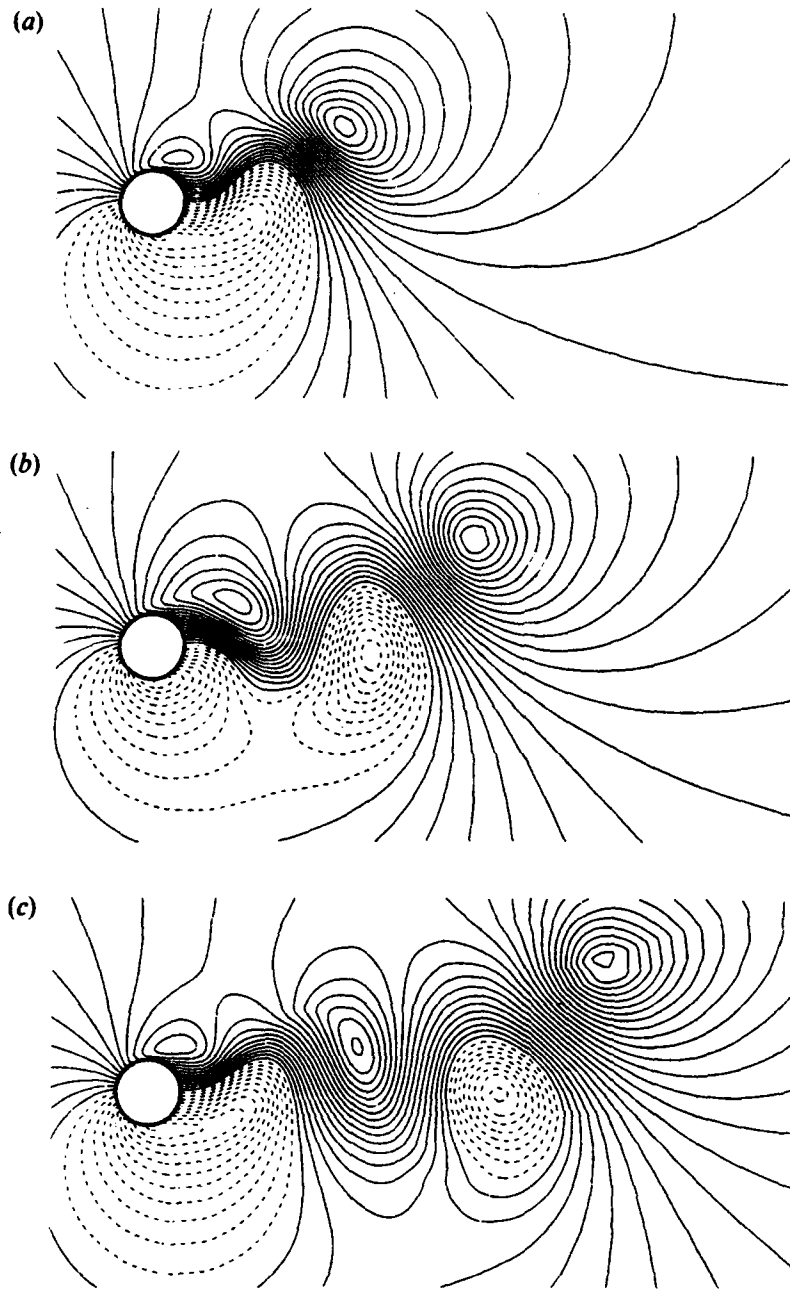
(a)

(b)

(c)

FIGURE 4. Instantaneous streamlines for $Re = 200$, $\alpha = 0.5$, viewed from a frame fixed with the undisturbed fluid. Dashed (solid) lines represent constant non-negative (negative) streamfunction values with increments of $\Delta\psi = \pm 0.1$, including $\psi = 0$. (a) $t = 12.0$, (b) 17.0, (c) 22.0.

For example, at $t = 7$, the streamwise location of the core of the first vortex is at about $x/a = 3.3$ as determined from the streamfunction (in a frame translating with the cylinder), and a bit less than $x/a = 2.5$ as determined from the vorticity. This clearly illustrates the effect of streamline masking on vortices moving with velocities significantly different than that of the frame to which the motion is referred.
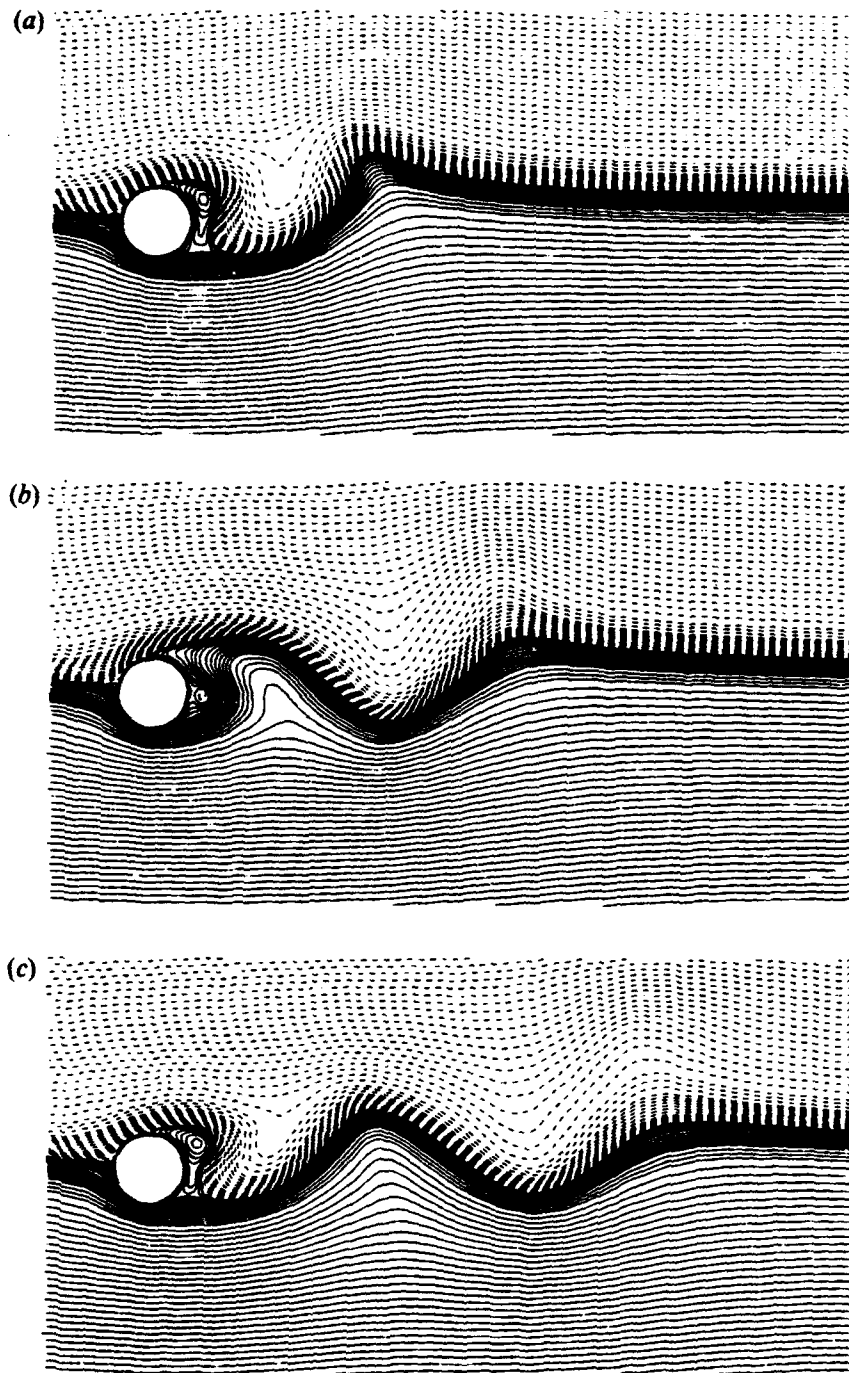
FIGURE 5. Instantaneous streamlines for $Re = 200$, $\alpha = 0.5$, viewed from the reference frame described in figure 3. The plotting convention and contour levels are as in figure 3. (a) $t = 12.0$, (b) 17.0, (c) 22.0.

The trajectories of figure 7(b) also show that the vortex cores execute motions much more complicated than would be inferred from the trajectories computed from streamfunction values (figure 7a of the present work and figure 4a of Badr & Dennis 1985). Specifically, for the first vortex core, figure 7(b) shows that although the x-component of the core velocity increases to nearly the free-stream value as the vortex moves farther behind the cylinder, the y-component oscillates (being sometimes negative) about a decidedly non-zero mean, to a distance at least 15 cylinder radii downstream.

As a further check on the accuracy of our results, we show in figure 8 the temporal evolution of profiles of the x-component of the velocity along the y-axis below the cylinder for $t \leqslant 8$. Very good quantitative agreement with experimental data taken from Coutanceau & Ménard (1985) is obtained near the cylinder. Farther away, there is slightly more scatter in the experimental data. Our results along the positive y-axis are graphically indistinguishable from those of Badr & Dennis (1985), obtained using different numerical methods.

5.2. Results for $\alpha = 1.0$

For $\alpha = 1.0$, we have computed streamlines analogous to those of figure 3(a–j) for $\alpha = 0.5$. Our results are indistinguishable from those of Badr & Dennis (1985) for the range of $t (1 \leqslant t \leqslant 12)$ covered in their work. For $14 \leqslant t \leqslant 24$, figure 9(a–f) shows instantaneous streamlines viewed from a non-rotating frame translating with the cylinder, beginning with the largest value of t considered in the experimental work of Coutanceau & Ménard (1985). Unlike the $\alpha = 0.5$ case where the second eddy E_2 appears at $t \approx 2.0$, here E_2 and the third intermediate eddy E_3' form almost simultaneously at $t \approx 6.5$, as shown in the earlier experimental and computational work. During the next cycle of vortex formation, however, E_4 appears before E_3'' is formed, as seen in figure 9(b, c). In general, the increase in α tends to inhibit the formation of the vortex at the downstream-moving side of the cylinder, as reported in previous experiments (Díaz *et al.* 1983; Coutanceau & Ménard 1985).

Figure 10(a–e) shows that the trajectories of the shed vortices for $\alpha = 1.0$ are qualitatively similar to those for $\alpha = 0.5$, except that the vortices shed from the downstream-moving side now lie above the midline of symmetry ($\theta = 0$), and due to the counterclockwise fluid motion generated near the cylinder by its rotation, will remain above the midline during their subsequent advection downstream. Otherwise, the topology of the shedding process is altered relatively little, with vortices of alternating sense being shed from opposite sides of the cylinder, and subsequently being found on opposite sides of an, albeit distorted, 'street' as they are advected downstream.

We have also computed the temporal evolution of profiles of the x- and y-components of the velocity along the x-axis in the wake of the cylinder for $t \leqslant 8$. Again, good agreement with the experimental results of Coutanceau & Ménard (1985) is obtained.

5.3. Results for $\alpha = 2.07$

As α increases, the vorticity layer generated at the upstream-moving side of the cylinder intensifies, resulting in even larger radial derivatives. Consequently, it becomes more difficult to maintain accuracy, as pointed out by Badr & Dennis (1985). We are able to achieve accurate numerical results by using finer radial grid spacings near the cylinder, as discussed in §3, and a smaller time-step size, as discussed at the beginning of this section. Figure 11(a–h) shows instantaneous streamlines in the near wake for
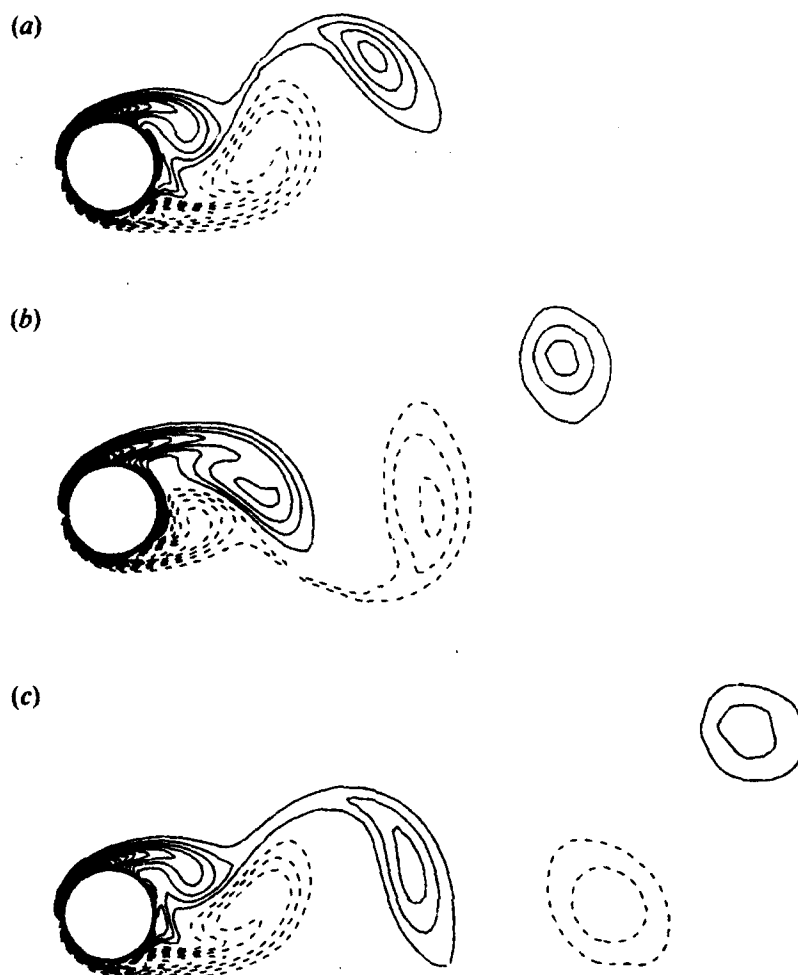
(a)

(b)

(c)

FIGURE 6. Equivorticity contours for $Re = 200$, $\alpha = 0.5$. Dashed (solid) lines represent constant positive (negative) vorticity values with a constant increment of ± 0.5, with the magnitude of the weakest contour level shown being 0.5. (a) $t = 12.0$, (b) 17.0, (c) 22.0.

$3 \leqslant t \leqslant 24$, viewed from a non-rotating frame translating with the cylinder. As seen in figure 12(a, b), our results are virtually identical to the flow visualizations of Coutanceau & Ménard (1985) for $t \leqslant 9$, the longest dimensionless time for which experimental results are available. The sequence of figures 13(a–d) for $t = 2$, 4, 6, and 8 shows that as t increases the computed flow is also in excellent agreement with experiment upstream of the cylinder, and becomes increasingly less symmetric about the x-axis.

The excellent agreement between our two-dimensional computations and the flow visualizations of Coutanceau & Ménard (1985) in a single spanwise plane strongly suggests that for $t \leqslant 9$ the flow is quite two-dimensional, at least near the centre of the span of the cylinder, and that sidewall boundary-layer effects are unimportant.

To better elucidate the vortex shedding process, we show in figure 14(a–f) the vorticity contours for $t \leqslant 24$. As for smaller values of α, vortex shedding still occurs for $\alpha = 2.07$, with vortices of alternating rotational sense shed from opposite sides of the cylinder. However, at this larger rotation rate the asymmetry of the process is clear.
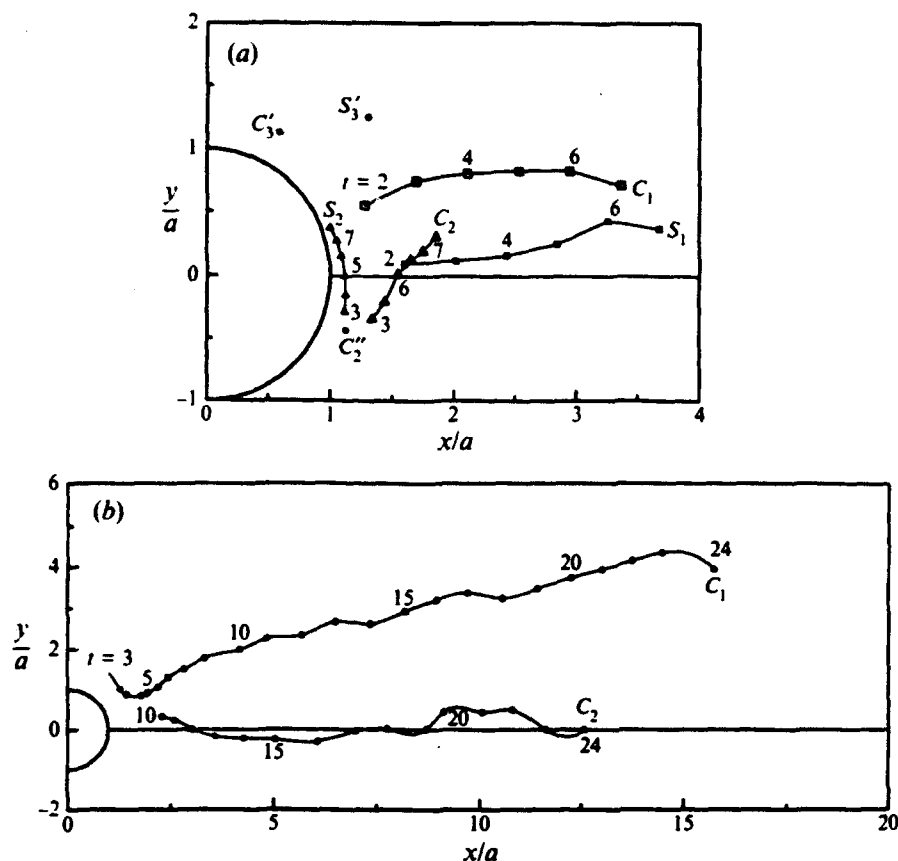
FIGURE 7. Trajectories of the cores C_i and closure points S_i for $Re = 200$, $\alpha = 0.5$ obtained from (*a*) instantaneous streamlines, and (*b*) equivorticity contours.

and manifests itself in the considerably reduced strength of the vortices shed from the downstream-moving side of the cylinder (relative to those for $\alpha = 0.5$ shown in figure 6*a–c*, and relative to those of opposite rotational sense for $\alpha = 2.07$), as well as in the fact that the shed vortices seem to be forming a 'single file' line, rather than pairing off (according to rotational sense) on opposite sides of a 'street'. The vortices shed from the downstream-moving side of the cylinder are relatively weak because immediately after the impulsive start, this part of the rotating boundary travels at about the same speed as the adjacent fluid. The weak vorticity layer generated near $\theta = \frac{3}{2}\pi$ (shown in figure 2*c*) is responsible for the weakness of the shed vortex.

Figure 15 shows that the trajectory of the vortex core C_1 determined from equivorticity contours is again very different from the trajectory determined by Coutanceau & Ménard from streamline data (their figure 14). In particular, the velocity of the first vortex core still has a considerable y-component until at least $t = 24$. This disagreement may be due to either the fact that the earlier determination of the vortex core trajectory was made from streamline data (discussed in §5.1), or to the 'confining wall effect' in the experimental work (discussed by Coutanceau & Ménard in conjunction with their results for $\alpha = 3.25$).
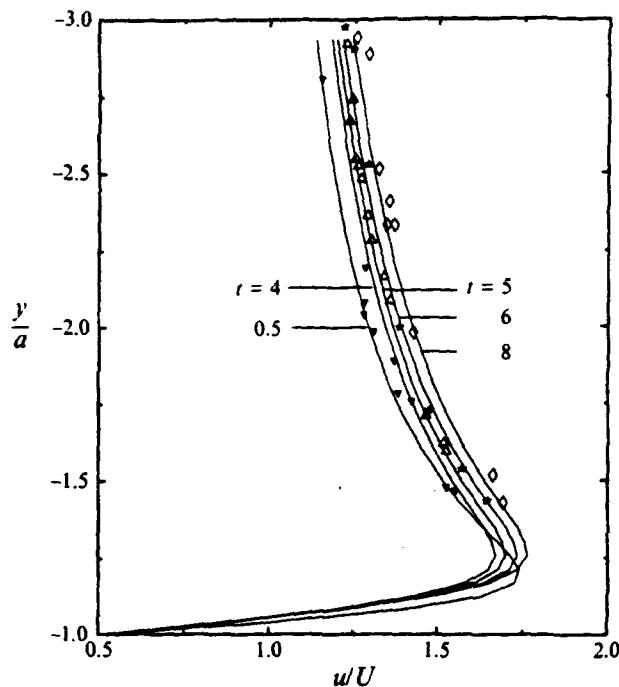
FIGURE 8. Temporal evolution of u-velocity profiles (in the frame described in figure 3) along the y-axis in the cylinder wake for $Re = 200$, $\alpha = 0.5$, $\theta = \frac{3}{4}\pi$. ——, Numerical solution. Symbols. experimental data of Coutanceau & Ménard (1985); ▼, $t = 0.5$; △, 4.0; ★, 5.0; ◇, 6.0.

5.4. Results for $\alpha = 3.25$

For $\alpha = 3.25$, figure 16$(a-d)$ shows instantaneous streamlines in the near wake for $t = 5, 9, 16,$ and 24, viewed from a non-rotating frame translating with the cylinder. In the same reference frame, figure 17$(a-d)$ shows comparisons of the computed streamlines to unpublished experimental results of Coutanceau & Ménard centred farther upstream. We note that the agreement (compare also figure 16b to figure 11d of Coutanceau & Ménard 1985), is very good. However, at $t = 9$ (the largest dimensionless time for which Coutanceau & Ménard reported results) the computational results differ perceptibly from the flow visualization of Coutanceau & Ménard (1985). We believe that the differences result from three-dimensional and sidewall boundary-layer effects in the experiments for large values of α at large time, as discussed by Coutanceau & Ménard (1985). Although for $\alpha = 0$ the nominally two-dimensional flow at $Re = 200$ is unstable with respect to three-dimensional disturbances (Williamson 1988); no information regarding the effect of rotation on stability appears to be available.

Computed vorticity contours are shown for $8 \leqslant t \leqslant 54$ in figure 18$(a-h)$. At $t = 24$, figure 18(c) shows that the elongated vorticity contour has not yet been severed. To investigate whether the vortex shedding process continues to larger t for this value of α, we let the size of the computational domain grow linearly in time until $t = 54$ in order to extend the computation. The same values of s_0 and s_1 in the stretching function are used to distribute 120 circular grid lines between $r = 1$ and $r = 1.5t - 12$. The numerical solution at $t = 54$ is not as accurate as at smaller dimensionless times since the vorticity at the outer perimeter ($r = 69$) is not negligible (on the order of 10^{-1} or
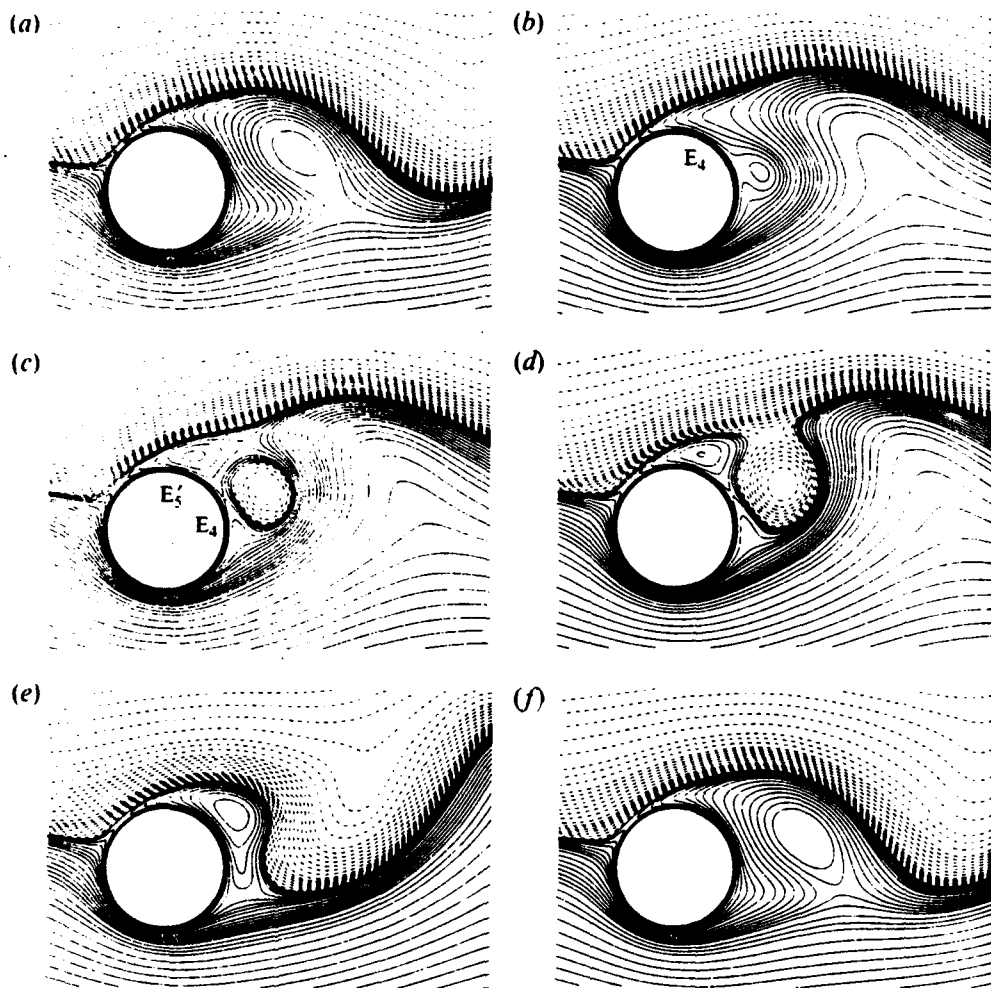
FIGURE 9. Instantaneous streamlines for $Re = 200$, $\alpha = 1.0$ at various times, viewed from the reference frame described in figure 3. The plotting convention and streamfunction values are as in figure 3. (a) $t = 14.0$, (b) 16.5, (c) 17.5, (d) 18.0, (e) 21.0, (f) 24.0.

smaller) at the end of the simulation. Nonetheless, we believe that our computation of the vortex shedding in the near wake is qualitatively correct, even for $t > 32$ (at which time the maximum of the absolute value of the vorticity on the outer boundary is still less than 4×10^{-4}).

Figure 18(e) shows that a second vortex is shed into the wake as for smaller α, although shedding here occurs at a much later time. However, even in a reference frame fixed with the undisturbed fluid, the weak second vortex is masked by the high velocity induced in the near wake by the rapidly rotating cylinder. Therefore, for large α it is not surprising that previous flow visualization experiments, including those performed in a frame translating with the cylinder, have failed to reveal the shedding of a second (weaker) vortex. Moreover, in the work of Coutanceau & Ménard (1985), experimental limitations prevented continuation of the flow to the dimensionless time at which the second vortex would have been shed. These difficulties have led to the erroneous conclusions that for $\alpha > 2.5$ (or $\alpha > 1$), no vortices are shed after the initial (strong) starting vortex, and that the vortex street is completely destroyed.
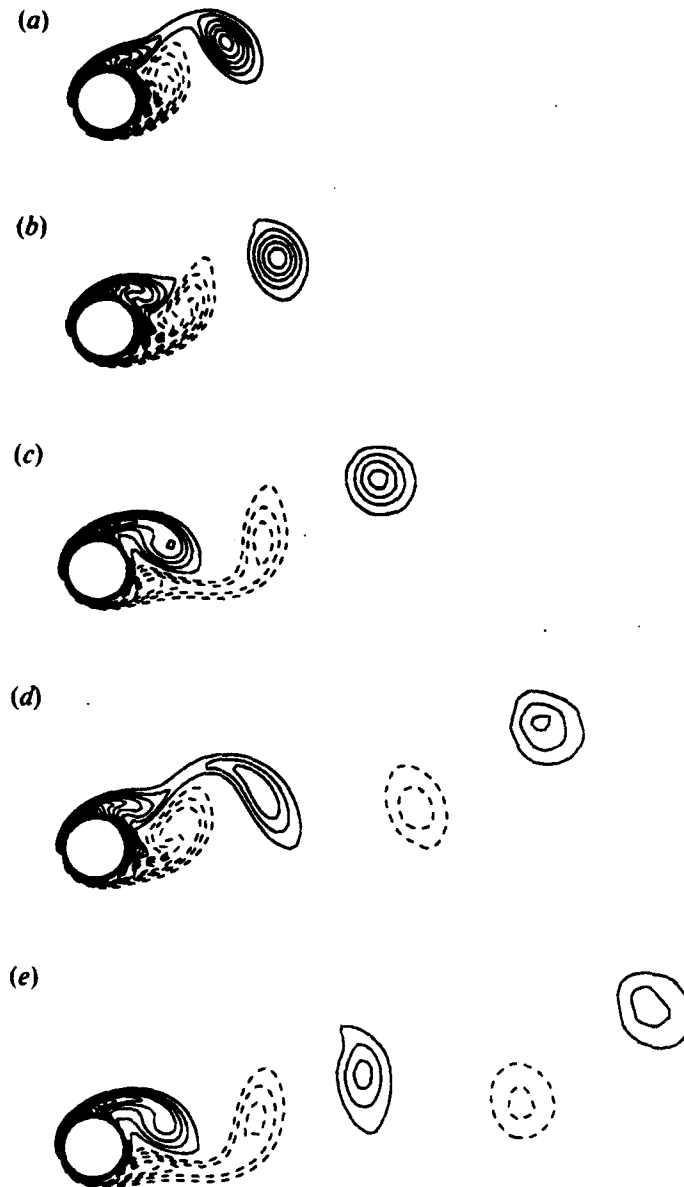
FIGURE 10. Equivorticity contours for $Re = 200$, $\alpha = 1.0$. Dashed (solid) lines represent constant positive (negative) vorticity values with a constant increment of 0.5, with the magnitude of the weakest contour level shown being 0.5. (a) $t = 8.0$, (b) 10.0, (c) 14.0, (d) 20.0, (e) 24.0.

To render the second vortex distinguishable using streamlines, we show in figure 19(a) the streamlines at $t = 32$ in a reference frame moving with the core of the second vortex. Experimentally, this would be a difficult task since a camera would have to move with the vortex core velocity vector $(u_c e_x + v_c e_y)$ relative to the cylinder, which is not known *a priori*. Numerically, this is achieved by simply subtracting streamfunction values corresponding to the velocity of the vortex core from those in an inertial reference frame fixed with the cylinder. The third vortex is clearly visible in
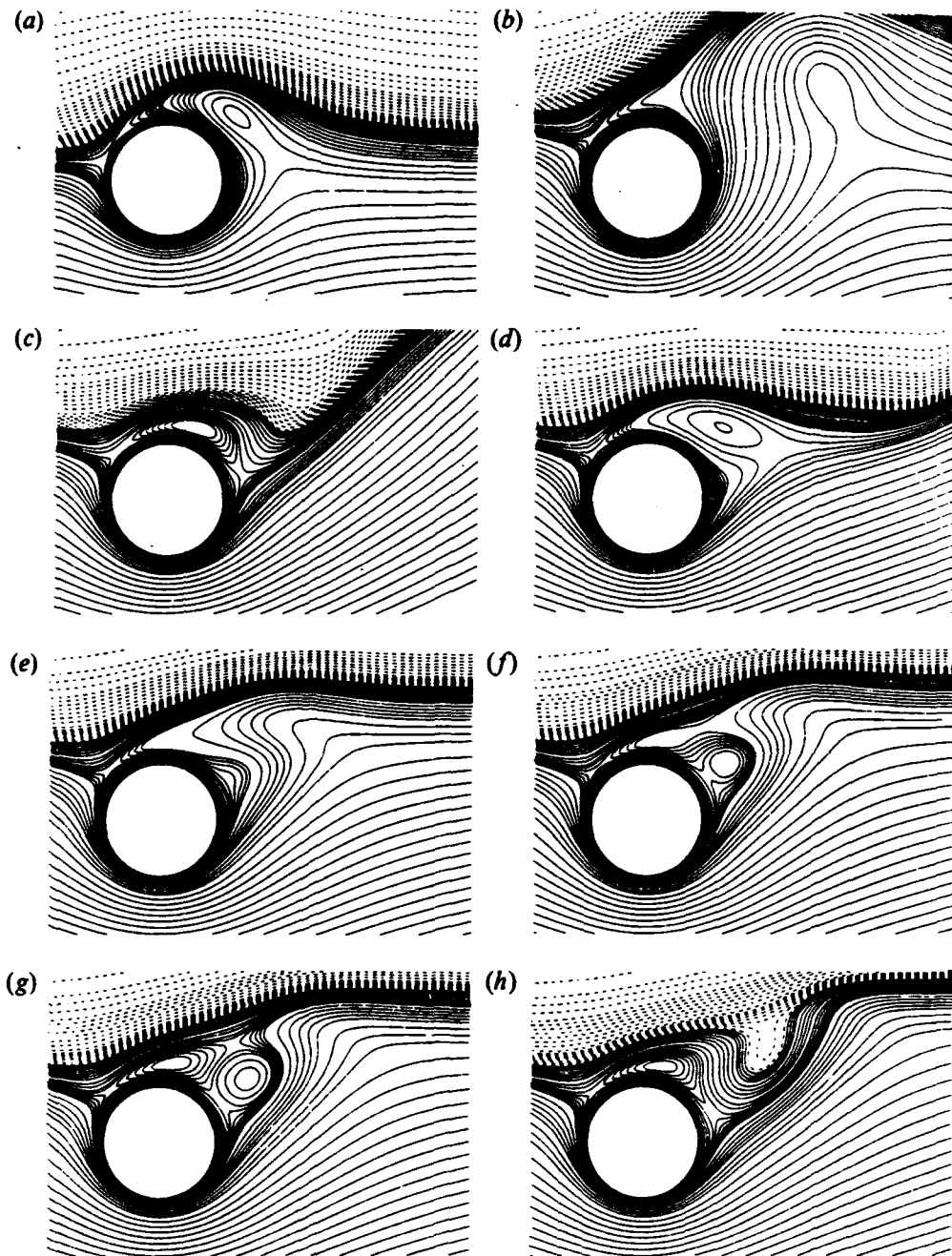
FIGURE 11. Instantaneous streamlines for $Re = 200$, $\alpha = 2.07$ at various times, viewed from the reference frame described in figure 3. In addition to those contour levels shown in figure 3, $\psi = -0.17$, -0.19, -0.21, -0.22, -0.23, -0.24 are also plotted. (a) $t = 3.0$, (b) 7.0, (c) 13.0, (d) 17.0, (e) 21.0, (f) 22.0, (g) 22.5, (h) 24.0.

a frame translating with its core (figure 19b), while the first vortex is still sufficiently strong to be discernible in this reference frame (in which its core velocity is non-zero).

In contrast to the results presented above for smaller α, for $\alpha = 3.25$ the third vortex shed is of the same rotational sense as the second. This differs from the case $Re = 10^3$
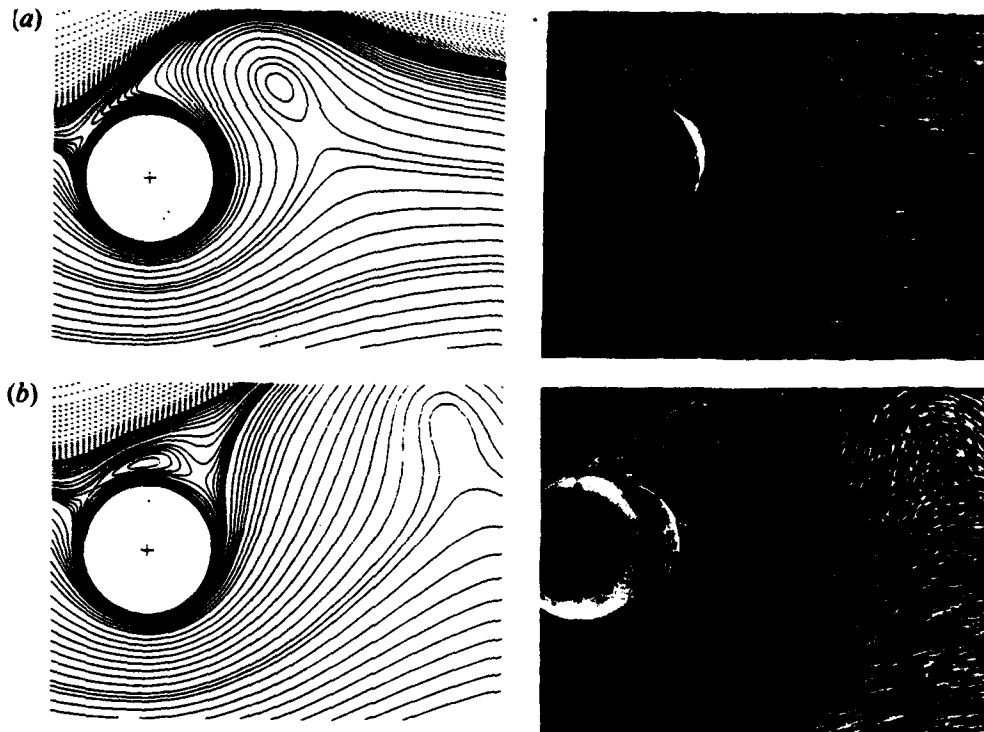
FIGURE 12. Comparison of computed (left) and experimental (right) instantaneous streamlines for $Re = 200$, $\alpha = 2.07$. The camera in the experiment and the reference frame in the computation translate with the cylinder. (a) $t = 5.0$, (b) $t = 9.0$.

and $\alpha = 3$ studied by Badr *et al.* (1990), in which the first two vortices formed are of the same sense, but only one is shed. Moreover, in the two-dimensional computations of Badr *et al.* (1990), only two vortices were formed, and the computed flow approached a steady state. With respect to understanding the real flow, however, their results must be regarded with caution, as the experiments of the same authors clearly show that the flow is three-dimensional for $Re = 10^3$ and $\alpha = 3$.

For $\alpha = 3.25$ the trajectory in figure 20 shows that, in the mean, the first vortex indeed continues to move upwards, in contrast to the result of Coutanceau & Ménard (their figure 14) in which the first vortex apparently moves back to the midline ($y = 0$). Coutanceau & Ménard ascribe this artifact to the effect of a confining (upper) wall, a complication not present in our computations.

5.5. Temporal evolution of the lift and drag coefficients

Finally, we present the temporal evolution of the lift and drag coefficients defined by

$$C_L = L/\rho U^2 a \tag{18}$$

and

$$C_D = D/\rho U^2 a, \tag{19}$$

where L and D are the lift and drag forces acting on the cylinder, respectively, and ρ is the density of the fluid. Integrating the pressure and shear stresses over the surface of the cylinder, we can express these in (r, θ)-coordinates as

$$C_L = C_{Lp} + C_{Lf} = \frac{2}{Re} \int_0^{2\pi} \left[-\left(\frac{\partial \omega}{\partial r}\right)_b + \omega_b \right] \cos\theta \, d\theta \tag{20}$$
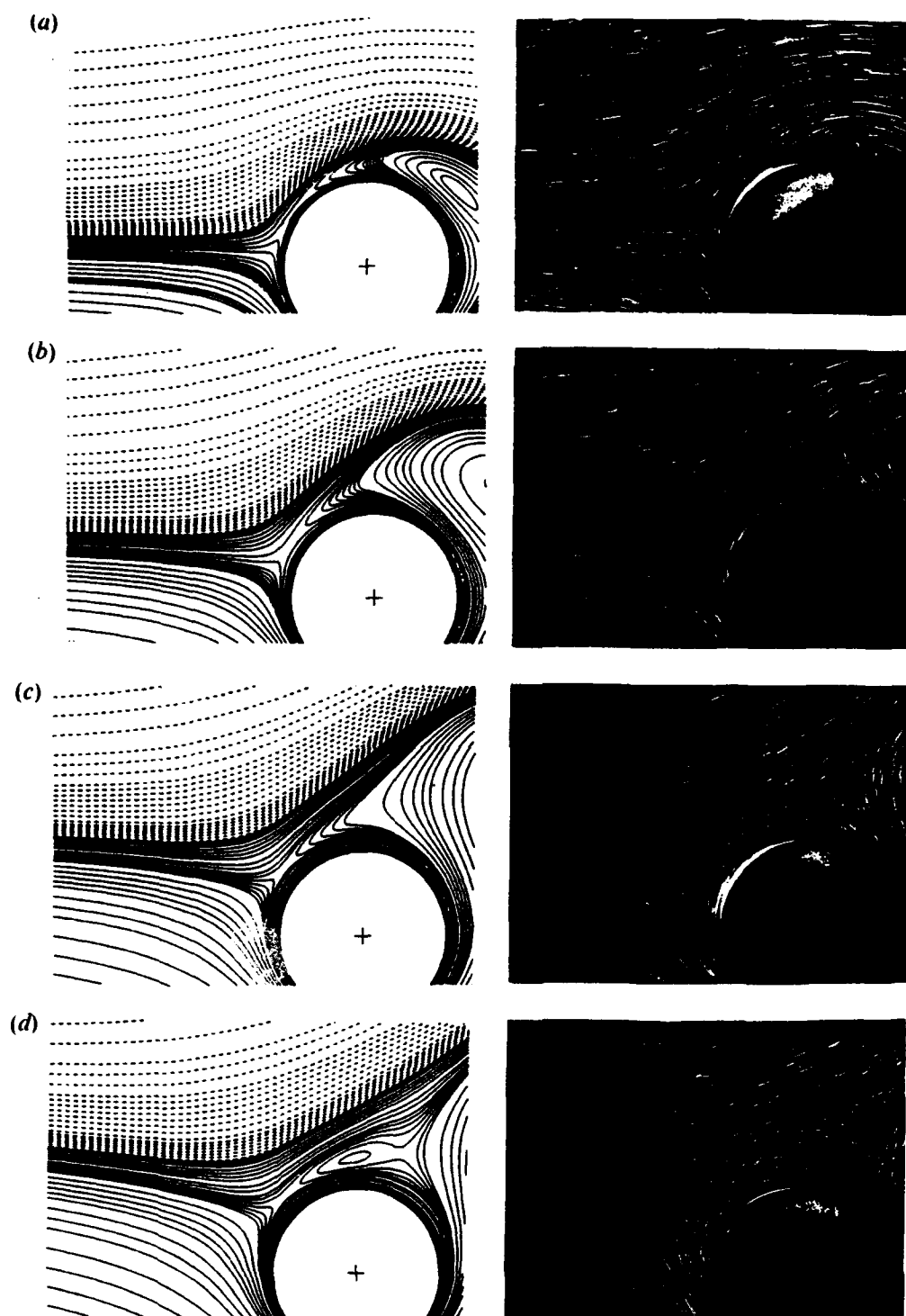
FIGURE 13. Comparison of computed (left) and experimental (right) instantaneous streamlines for $Re = 200$, $\alpha = 2.07$. Reference frame and camera motion are as described in figure 12. (a) $t = 2.0$, (b) 4.0, (c) 6.0, (d) 8.0.
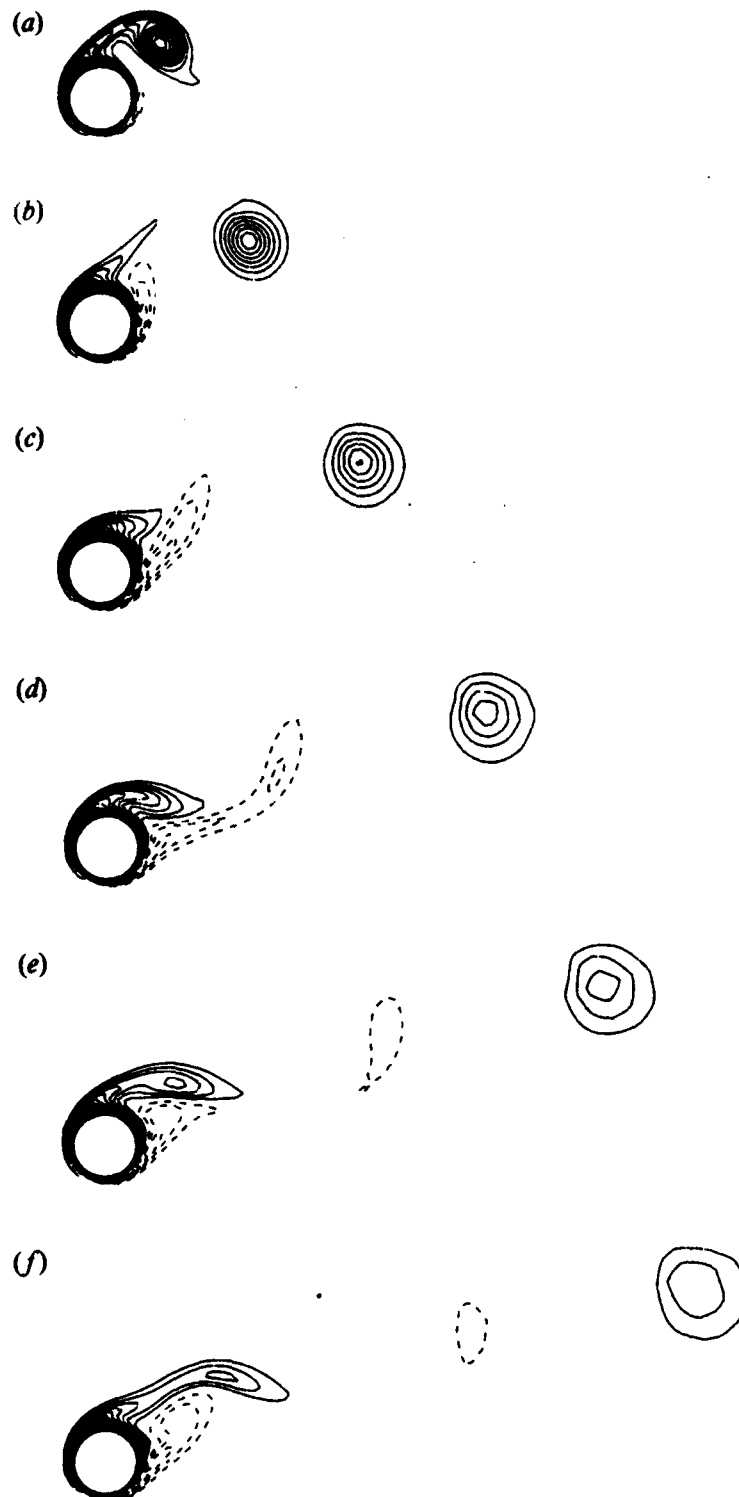
FIGURE 14. Equivorticity contours for $Re = 200$, $\alpha = 2.07$. Dashed (solid) lines represent constant positive (negative) vorticity values with a constant increment of 0.5, with the magnitude of the weakest contour level shown being 0.5. (a) $t = 5.0$, (b) 9.0, (c) 13.0, (d) 17.0, (e) 21.0, (f) 24.0.
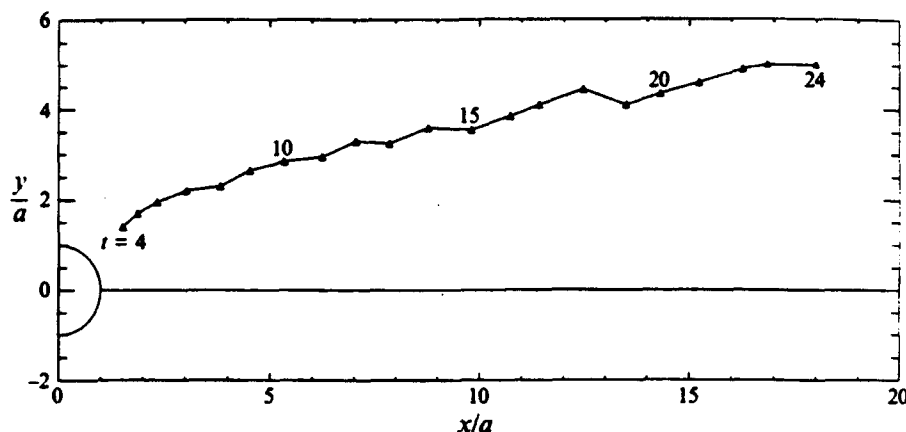
FIGURE 15. Trajectory of the core of the first vortex for $Re = 200$, $\alpha = 2.07$
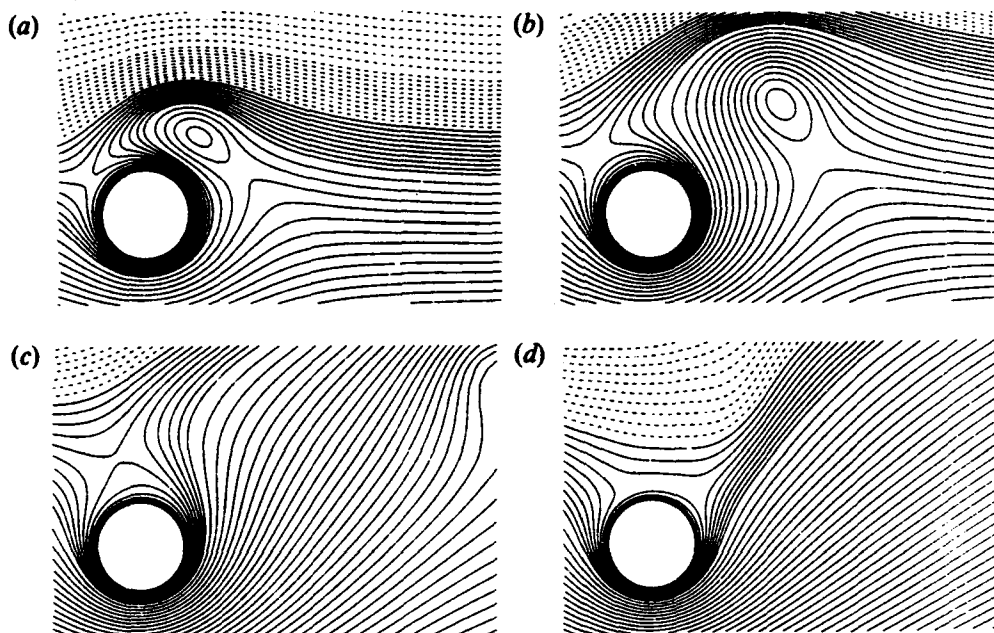obtained from equivorticity contours.

FIGURE 16. Instantaneous streamlines for $Re = 200$, $\alpha = 3.25$ at various times, viewed from the reference frame described in figure 3. The plotting convention is as in figure 3. The values of ψ plotted are 0, ± 0.1, ± 0.2, ± 0.3, ± 0.4, ± 0.5, ± 0.6, ± 0.7, ± 0.8, ± 0.9, ± 1.0, with an increment of ± 0.2 thereafter. (a) $t = 5.0$, (b) 9.0, (c) 16.0, (d) 24.0.

$$\text{and} \qquad C_D = C_{Dp} + C_{Df} = \frac{2}{Re} \int_0^{2\pi} \left[\left(\frac{\partial \omega}{\partial r} \right)_b - \omega_b \right] \sin \theta \, d\theta, \qquad (21)$$

where the subscripts p and f denote contributions due to the pressure and friction, respectively, and the subscript b denotes quantities evaluated on the cylinder. We note that (20) and (21) differ from the expressions given by Badr et al. (1989) by a sign, due to a difference in the definition of vorticity. Figure 21(a, b) shows the temporal evolution of the lift and drag coefficients at various α for $t \leqslant 24$. Negative values of C_L
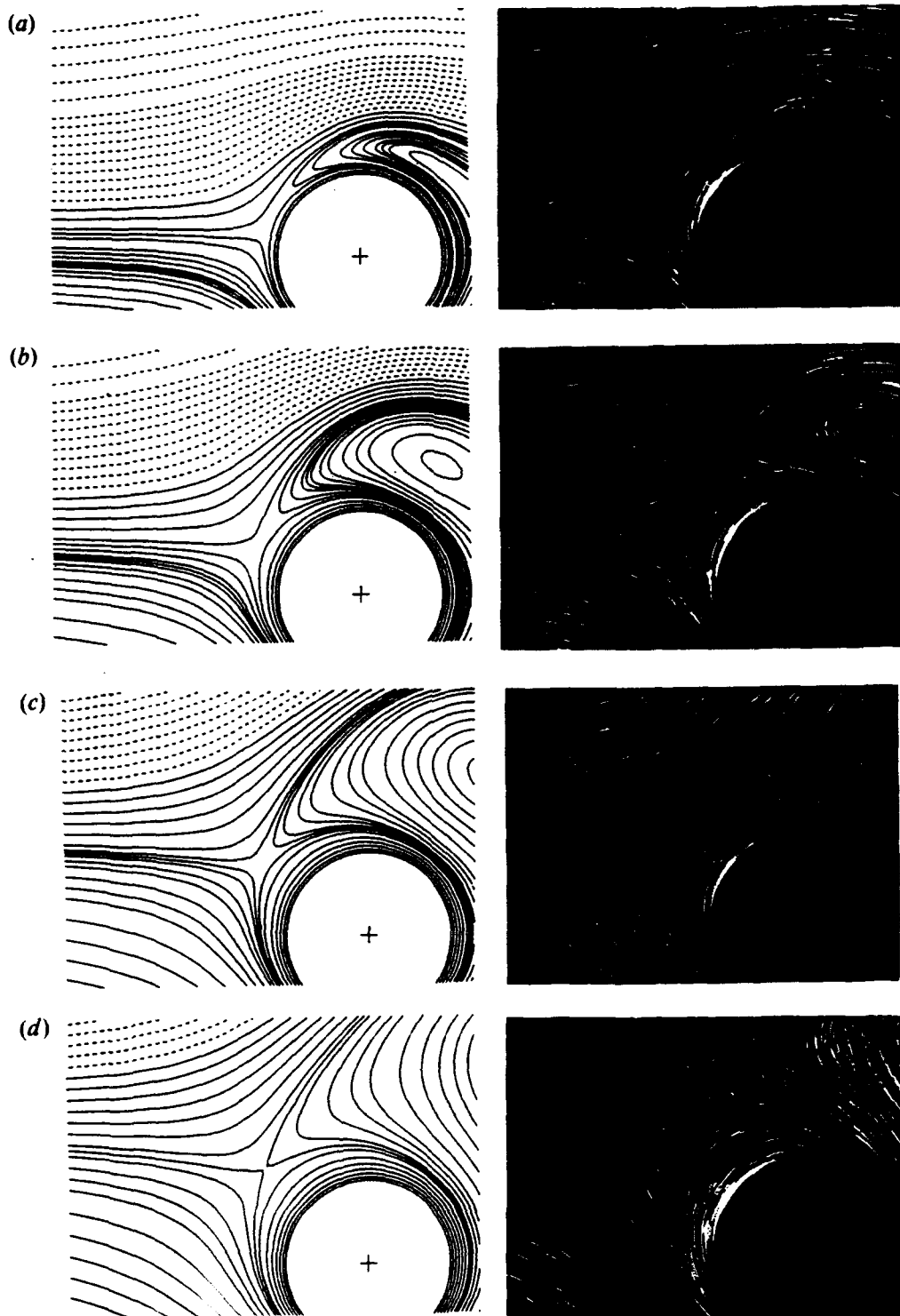
FIGURE 17. Comparison of computed (left) and experimental (right) instantaneous streamlines for $Re = 200$, $\alpha = 3.25$. Reference frame and camera motion are as described in figure 12. (*a*) $t = 2.0$, (*b*) 4.0, (*c*) 6.0, (*d*) 8.0.
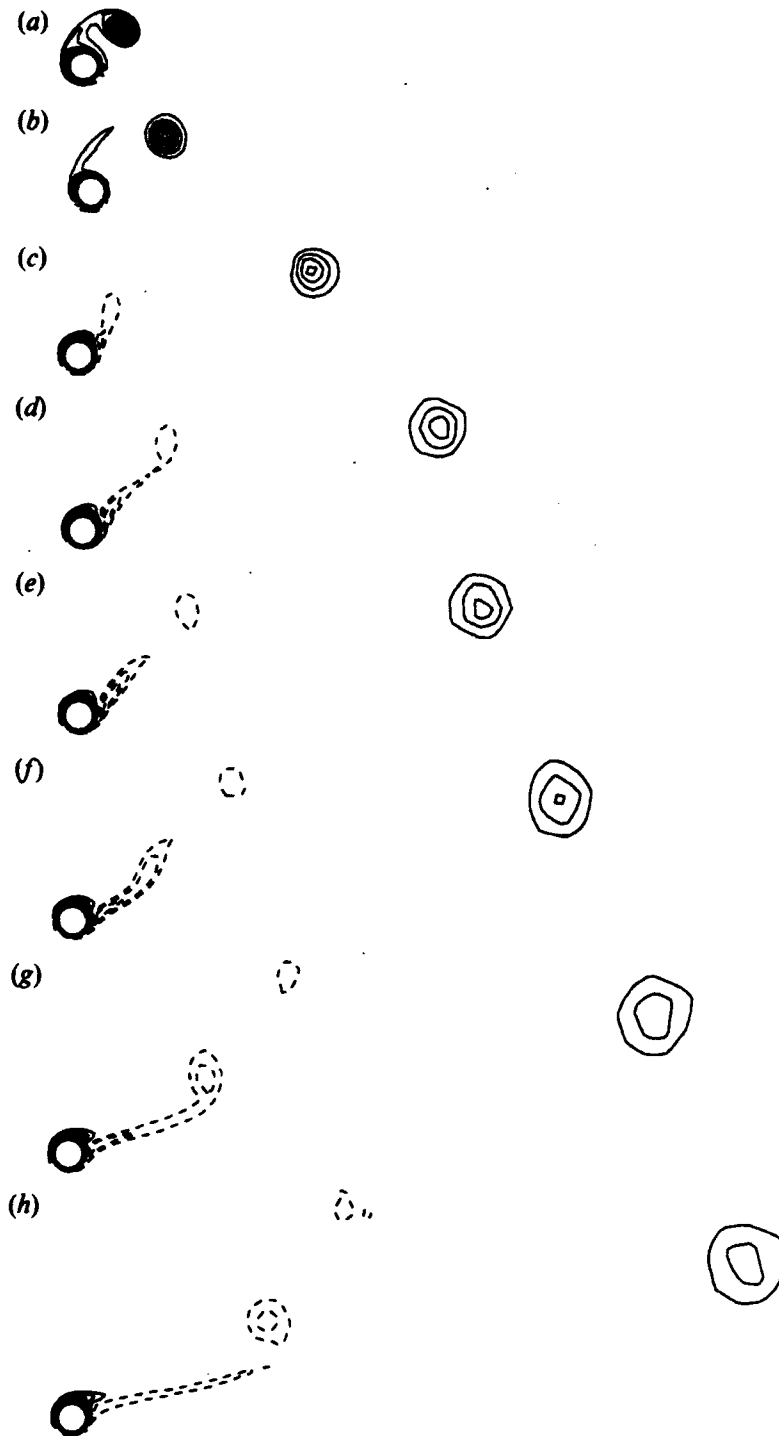
FIGURE 18. Equivorticity contours for $Re = 200$, $\alpha = 3.25$. Dashed (solid) lines represent constant positive (negative) vorticity values with a constant increment of 0.5, with the magnitude of the weakest contour level shown being 0.5. (a) $t = 8.0$, (b) 12.0, (c) 24.0, (d) 32.0, (e) 35.0, (f) 41.0, (g) 48.0, (h) 54.0.
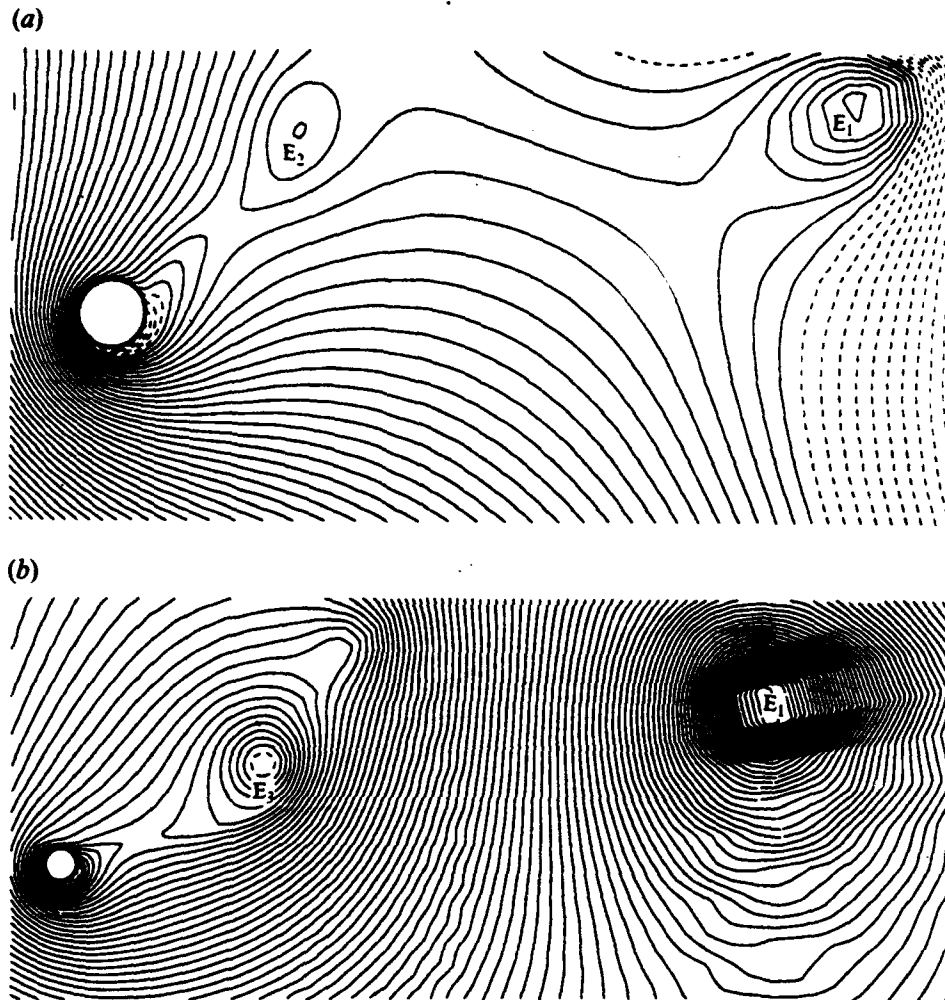
(a)

(b)

FIGURE 19. Instantaneous streamlines for $Re = 200$, $\alpha = 3.25$: (a) $t = 32.0$, viewed from a frame translating with the core of the second vortex; (b) $t = 54.0$, viewed from a frame translating with the core of the third vortex. Dashed (solid) lines represent constant non-negative (negative) streamfunction values with increments of $\Delta\psi = 0.2$, including $\psi = 0$. Note that in (b), eddy E_2 has passed from the field of view.

correspond to a lift force in the negative y-direction. The time-periodic nature of C_L is well established for $\alpha = 0.5$ and 1.0. At higher values of α, however, more time is required for periodicity to be established, since the second and subsequent eddies form and are shed much later, as discussed above. In figure 22(a, b), the pressure and skin friction contributions to the lift and drag are shown separately for $\alpha = 1.0$. Similarly small viscous contributions to C_L and C_D are found for all other values of α investigated. It is clear that lift and drag are largely due to the pressure force, consistent with previous work showing that the Magnus effect is primarily an inviscid phenomenon.

6. Discussion

Our computations of the temporal development of the flow generated by a circular
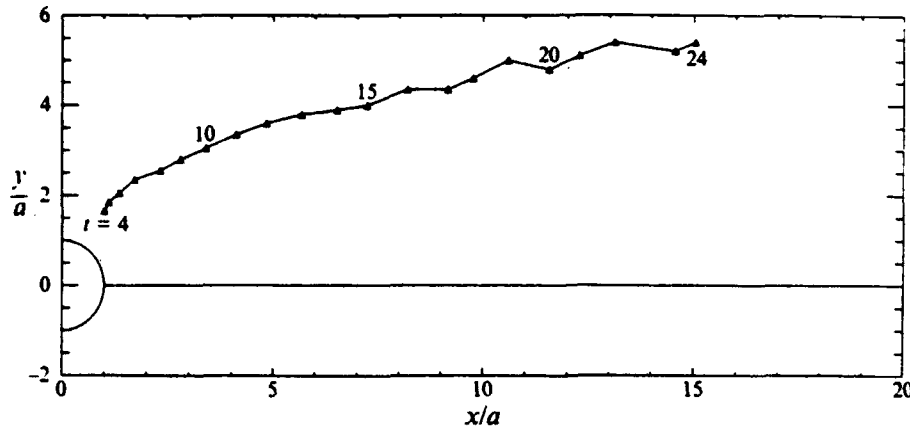
FIGURE 20. Trajectory of the core of the first vortex for $Re = 200$, $\alpha = 3.25$ obtained from equivorticity contours.

cylinder started impulsively from rest into steady rotatory and rectilinear motion at $Re = 200$ show that, for the largest value of α (3.25) investigated by Coutanceau & Ménard (1985), vortex shedding continues after the first vortex is shed. contrary to earlier conclusions. It is likely that these authors were led to conclude that vortex shedding at $Re = 200$ is suppressed for $\alpha \gtrsim 2$ because their experimental facility did not allow for visualization of the flow for a long enough time. Even if that limitation had been overcome, however, it is likely that their flow visualization technique (which approximately yields instantaneous streamlines) would have failed to reveal the presence of the second vortex, due to masking by the large velocities induced in the near wake by the rapidly rotating cylinder.

We note that for $\alpha = 3.25$ the time interval between the shedding of the first and second vortices is much longer than the time required to shed the first. We conjecture that for subsequent vortices, the interval between shedding of the $2n$th and $(2n+1)$th vortices will be considerably shorter than the interval between shedding of the $(2n+1)$th and $(2n+2)$th.

We also observe that for $\alpha = 2.07$ and 3.25 the second vortex (shed from the downstream-moving side of the cylinder) is much smaller than the first, and conjecture that, in general, the $2n$th vortex shed will be significantly smaller than the $(2n+1)$th. Unlike the non-rotating ($\alpha = 0$) case, there is no requirement that the vortices shed from opposite sides of the cylinder be of equal magnitude, or even that consecutive vortices be shed alternately from opposite sides of the cylinder. In fact, there does not appear to be any reason why vortices cannot be shed from a single (upstream-moving) side of the cylinder.

From a more general standpoint, we can consider the computational and experimental results in the broader context of three-dimensional flows. For this purpose, it is useful to characterize the asymptotic stability of the flow in terms of a translational Reynolds number defined by $Re_t = 2aU/\nu$ and a rotational Reynolds number defined by $Re_r = 2a^2\Omega/\nu$, equivalent to Re and αRe, respectively. Thus, uniform flow past a rotating circular cylinder can be considered in the (Re_t, Re_r)-plane, a quarter of which is shown in figure 23. From the computational results of Jackson (1987) and Zebib (1987) and the experimental work cited therein, we know that uniform steady two-dimensional flow past a non-rotating cylinder ($Re_r = 0$) is stable for $Re_t \lesssim 45$, at which point a supercritical Hopf bifurcation to a time-periodic two-
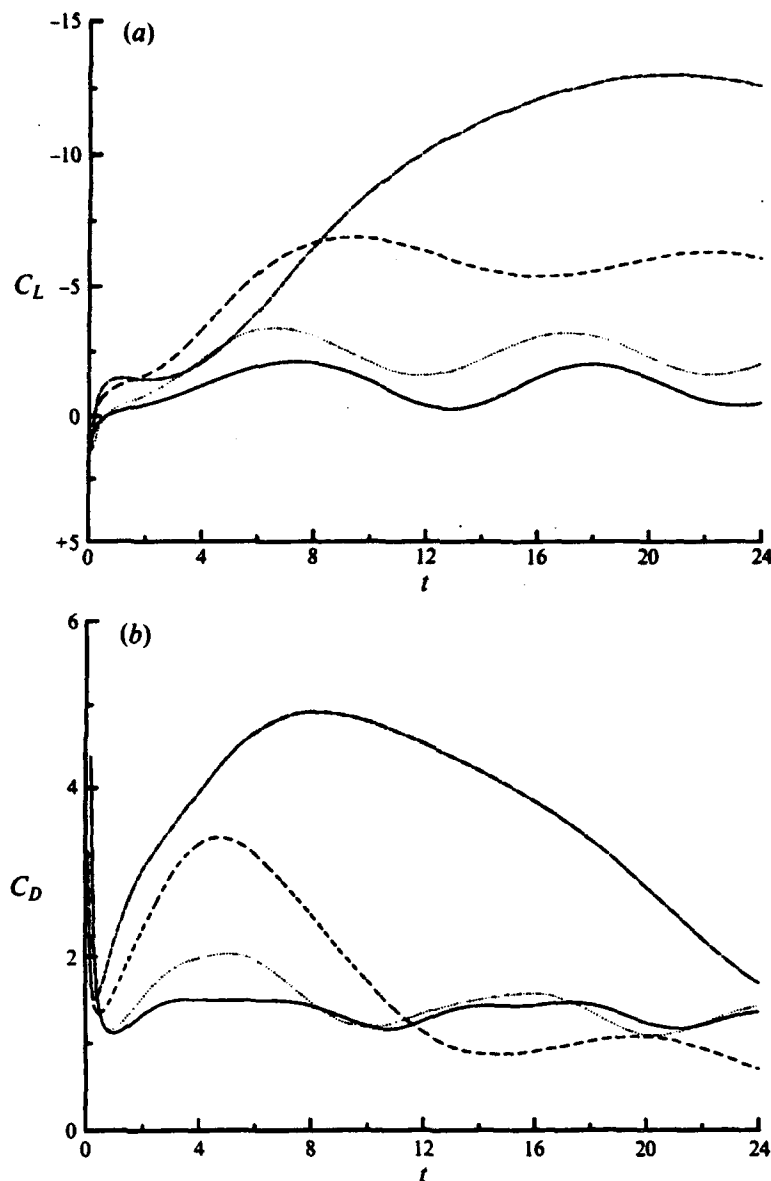
FIGURE 21. Temporal evolution of (a) the lift and (b) drag coefficients for $Re = 200$ and various α for $0 \leqslant t \leqslant 24$; ———, $\alpha = 0.5$; ......, $\alpha = 1.0$; ------, $\alpha = 2.07$; —·—·—·, $\alpha = 3.25$.

dimensional oscillating wake flow occurs. On the other hand, for a circular cylinder undergoing steady rotation only ($Re_t = 0$), Walowit, Tsao & DiPrima (1964) have shown that the steady purely azimuthal flow ($V = e_\theta \Omega a^2/r$) is linearly stable for $Re_r \lesssim 11$, at which point it becomes unstable with respect to a steady axisymmetric flow consisting of Taylor vortices.

We therefore conjecture that steady two-dimensional flows past a rotating circular cylinder are stable with respect to infinitesimally small but otherwise arbitrary disturbances in a region (I in figure 23) of the (Re_t, Re_r)-quarter-plane including the origin. As the curve (shown schematically and referred to below as the 'stability
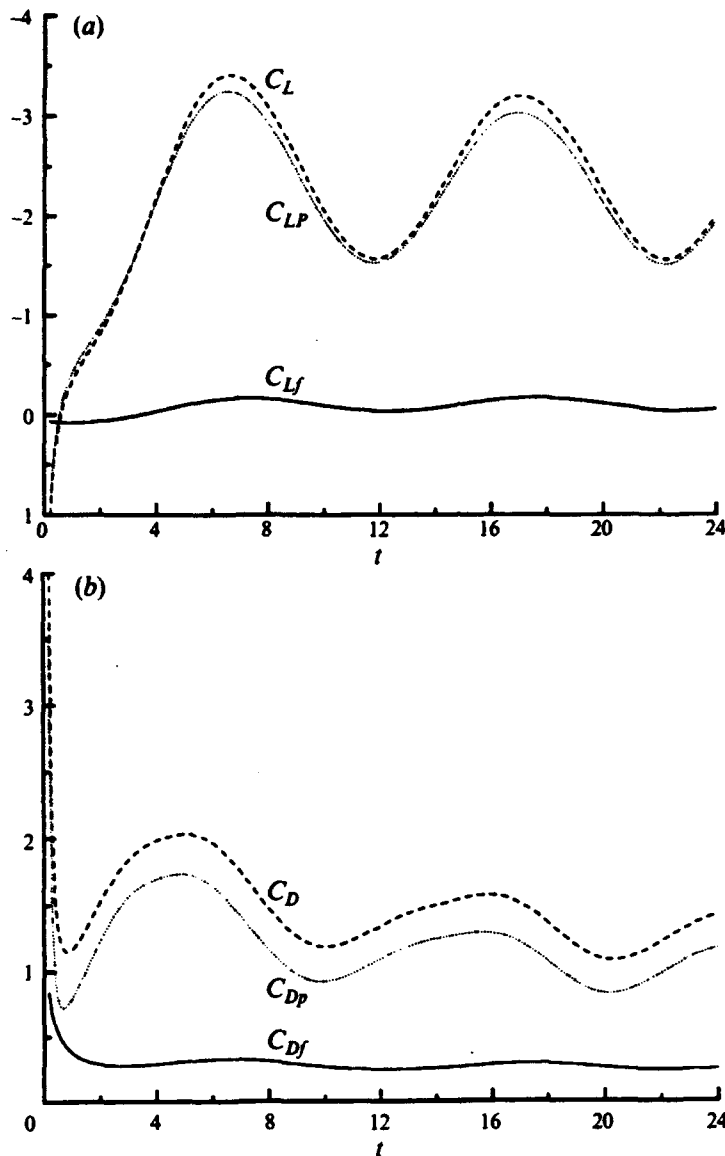
FIGURE 22. Contributions of pressure and skin friction to (a) lift and (b) drag for $Re = 200$ and $\alpha = 1.0$ for $0 \leqslant t \leqslant 24$; ——, skin friction; ......, pressure; ––––––, total.

boundary') bounding Region I is crossed, we propose that for small α (note that α is the slope of a line connecting the origin to a point in the quarter-plane) the ensuing motion is time-periodic and two-dimensional, while for large α it is steady and three-dimensional (axisymmetric in the limit $Re_t \rightarrow 0$). It would thus appear that

(a) there exists at least one point on the stability boundary at which the nature of the bifurcation from steady two-dimensional flow changes, and

(b) there exist two regions adjacent to I, in which an unsteady two-dimensional flow should be realizable (Region II) and in which a steady three-dimensional flow should be realizable (Region III).

Although it is known for $Re_r = 0$ (Williamson 1988) and for $Re_r \neq 0$ (Badr et al.
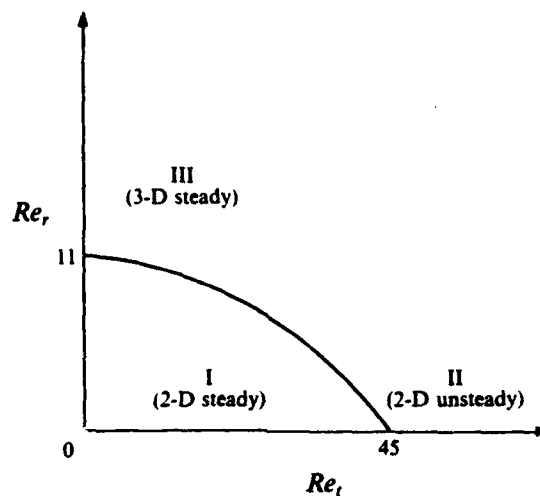
FIGURE 23 Schematic division of the (Re_t, Re_r)-quarter-plane. Two-dimensional steady solutions are stable in region I. Regions II and III are described in the text.

1990) that the unsteady two-dimensional flow becomes unstable with respect to unsteady three-dimensional flows at sufficiently high Re_t, the bifurcation structure remains to be determined. Among the questions to be answered are

(i) If Regions II and III have a common boundary, how does a transition occur from unsteady two-dimensional flow to steady three-dimensional flow?

(ii) If Regions II and III do not have a common boundary, what lies between them?

(iii) How does the bifurcation from steady two-dimensional flow change along the stability boundary?

From the standpoint of controlling laminar two-dimensional vortex shedding from a circular cylinder by using either 'active' control (a term that in the fluid mechanics literature has come to mean a time-periodic, and frequently harmonic input, e.g. $\Omega(t + T) = \Omega(t)$ or $\Omega(t) = \Omega_0 \sin 2\pi ft$) or feedback control, the present calculations show that the nature of the vorticity field as well as the vortex shedding process can be significantly altered by cylinder rotation. To the best of our knowledge, the only investigations to date concerning the effect of a time-dependent rotation rate on the shedding process are the experimental studies of Taneda (1977, 1978) and Tokumaru & Dimotakis (1991), and the combined experimental and theoretical studies of Okajima, Takata & Asanuma (1975), Mo (1989), and Wu, Mo & Vakili (1989).

The experimental work of Taneda (1978) for $30 \leqslant Re \leqslant 300$ (including the range in which Hopf bifurcation (Jackson 1987; Zebib 1987) of the steady two-dimensional flow at $Re \approx 45$ leads to unsteady asymmetric two-dimensional solutions exhibiting vortex shedding) shows that for sufficiently large values of the amplitude and frequency of time-harmonic rotatory oscillations, vortex shedding (and indeed the formation of attached vortices) can be eliminated. Moreover, Taneda's flow visualizations (see his figure 3d) indicate that under certain circumstances, a flow can be generated that is nearly symmetric about $\theta = 0$. This suggests that the flow can be driven to a symmetric state, and provides reason to believe that it can be stabilized (in the control-theoretical sense; cf. Kuo 1975) about a symmetric state in which no vortex shedding occurs.

REFERENCES

BADR, H. M. & DENNIS, S. C. R. 1985 Time-dependent viscous flow past an impulsively started rotating and translating circular cylinder. *J. Fluid Mech.* **158**, 447–488.

BADR, H. M., DENNIS, S. C. R. & YOUNG, P. J. S. 1989 Steady and unsteady flow past a rotating circular cylinder at low Reynolds numbers. *Computers & Fluids* **17**, 579–609.

BADR, H., COUTANCEAU, M., DENNIS, S. & MÉNARD, C. 1986 On the phenomenon of vortex transposition of coalescence in separated flows. *C. R. Acad. Sci. Paris* **302**(II), 1127–1130.

BADR, H. M., COUTANCEAU, M., DENNIS, S. C. R. & MÉNARD, C. 1990 Unsteady flow past a rotating circular cylinder at Reynolds numbers 10^3 and 10^4. *J. Fluid Mech.* **220**, 459–484.

CHANG, C.-C. & CHERN, R.-L. 1992 Vortex shedding from an impulsively started rotating and translating cylinder. *J. Fluid Mech.* **235**, 265–298.

CHEN, Y.-M. 1989 Numerical simulation of the unsteady two-dimensional flow in a time-dependent doubly-connected domain. PhD dissertation, University of Arizona.

CHEN, Y.-M., KONIGES, A. E. & ANDERSON, D. V. 1989 ILUBCG2-11: Solution of 11-banded nonsymmetric linear equation systems by a preconditioned biconjugate gradient routine. *Comput. Phys. Commun.* **55**, 359–365.

COLLINS, W. M. & DENNIS, S. C. R. 1973 Flow past an impulsively started circular cylinder. *J. Fluid Mech.* **60**, 105–127.

COUTANCEAU, M. & MÉNARD, C. 1985 Influence of rotation on the near-wake development behind an impulsively started circular cylinder. *J. Fluid Mech.* **158**, 399–446.

DÍAZ, F., GAVALDÁ, J., KAWALL, J. G., KEFFER, J. F. & GIRALT, F. 1983 Vortex shedding from a spinning cylinder. *Phys. Fluids* **26**, 3454–3460.

EATON, B. E. 1987 Analysis of laminar vortex shedding behind a circular cylinder by computer-aided flow visualization. *J. Fluid Mech.* **180**, 117–145.

FASEL, H. 1976 Investigation of the stability of boundary layers by a finite-difference model of the Navier–Stokes equations. *J. Fluid Mech.* **78**, 355–383.

FORNBERG, B. 1980 A numerical study of steady viscous flow past a circular cylinder. *J. Fluid Mech.* **98**, 819–855.

GLAUERT, M. B. 1957*a* A boundary layer theorem, with applications to rotating cylinders. *J. Fluid Mech.* **2**, 89–99.

GLAUERT, M. B. 1957*b* The flow past a rapidly rotating circular cylinder. *Proc. R. Soc. Lond.* A **242**, 108–115.

INGHAM, D. B. 1983 Steady flow past a rotating cylinder. *Computers & Fluids* **11**, 351–366.

INGHAM, D. B. & TANG, T. 1990 A numerical investigation into the steady flow past a rotating circular cylinder at low and intermediate Reynolds numbers. *J. Comput. Phys.* **87**, 91–107.

JACKSON, C. P. 1987 A finite-element study of the onset of vortex shedding in flow past variously shaped bodies. *J. Fluid Mech.* **182**, 23–45.

KIMURA, T., TSUTAHARA, M. & WANG, Z. 1992 Wake of a rotating circular cylinder. *AIAA J.* **30**, 555–556.

KLEWICKI, J. C. & FALCO, R. E. 1991 On accurately measuring statistics associated with small-scale turbulent boundary layers using hot-wire probes. *J. Fluid Mech.* **219**, 119–142.

KOROMILAS, C. A. & TELIONIS, D. P. 1980 Unsteady laminar separation: an experimental study. *J. Fluid Mech.* **97**, 347–384.

KRAHN, E. 1955 The laminar boundary layer on a rotating cylinder in crossflow. *NAVORD Rep.* 4022.

KUO, B. 1975 *Automatic Control Systems*, 3rd Edn. Prentice-Hall.

LUGT, H. J. 1979 The dilemma of defining a vortex. In *Recent Developments in Theoretical and Experimental Fluid Mechanics* (ed. U. Müller, K. G. Roesner & B. Schmidt), pp. 309–321. Springer.

LUGT, H. J. & HAUSSLING, H. J. 1974 Laminar flow past an abruptly accelerated elliptic cylinder at 45° incidence. *J. Fluid Mech.* **65**, 711–734.

LYULKA, V. A. 1977 Numerical solution of the problem of the rotation of a cylinder in a flow of a viscous incompressible fluid. *Vyschisl. Mat. mat. Fiz.* **17**, 470–480. (Translated in *USSR Comput. Maths and Math. Phys.* **17** (2), 178–188, 1978.)

MO, J. 1989 An investigation of wake flow around a cylinder with rotational oscillations. PhD dissertation, University of Tennessee Space Institute.

MODI, V. J., MOKHTARIAN, F. & YOKOMIZO, T. 1990 Effect of moving surfaces on the airfoil boundary-layer control. *J. Aircraft* **27**, 42–50.

MOORE, D. W. 1957 The flow past a rapidly rotating cylinder in a uniform stream. *J. Fluid Mech.* **2**, 541–550.

OKAJIMA, A., TAKATA, H. & ASANUMA, T. 1975 Viscous flow around a rotationally oscillating circular cylinder. *Rep.* 532. Institute of Space and Aeronautical Science, University of Tokyo.

ORSZAG, S. A. 1980 Spectral methods for problems in complex geometries. *J. Comput. Phys.* **37**, 70–92.

PAYNE, R. B. 1958 Calculations of unsteady flow past a circular cylinder. *J. Fluid Mech.* **4**, 81–86.

PERRY, A. E., CHONG, M. S. & LIM, T. T. 1982 The vortex-shedding process behind two-dimensional bluff bodies. *J. Fluid Mech.* **116**, 77–90.

PRANDTL, L. 1925 The Magnus effect and windpowered ships. *Naturwissenschaften* **13**, 93–108.

PRANDTL, L. & TIETJENS, O. G. 1934 *Applied Hydro- and Aeromechanics* (transl. J. P. Den Hartog 1957). Dover.

REDDY, R. N. & THOMPSON, J. F. 1977 Numerical solution of incompressible Navier–Stokes equations in the integro-differential formulation using boundary-fitted coordinate systems. *AIAA Paper* 77-650.

SHKADOVA, V. P. 1982 Rotating cylinder in a flowing viscous incompressible fluid. *Akad. Nauk SSSR, Izv. Mekh. Zhidk. Gaza* (1), 16–21. (Translated in *Fluid Dyn.* **17** (1), 12–16, 1982.)

SIMUNI, L. M. 1967 Solution of certain problems in flow of a viscous fluid, associated with a cylinder and a sphere. *Izv. Sib. Otdel. Akad. Nauk SSSR, Ser. Tekh. Nauk.* (2), 23–28.

SWANSON, W. M. 1961 The Magnus effect: a summary of investigations to date. *Trans. ASME D: J. Basic Engng* **83**, 461–470.

TA PHUOC LOC 1975 Étude numérique de l'écoulement d'un fluide visqueux incompressible autour d'un cylindre fixe ou en rotation. Effet Magnus. *J. Méc.* **14**, 109–134.

TANEDA, S. 1977 Visual study of unsteady separated flows around bodies. *Prog. Aero. Sci.* **17**, 287–348.

TANEDA, S. 1978 Visual observations of the flow past a circular cylinder performing a rotatory oscillation. *J. Phys. Soc. Japan* **45**, 1038–1043.

TANEDA, S. 1980 Visualization of unsteady flow separation. In *Flow Visualization II* (ed. W. Merzkirch), pp. 253–257. Hemisphere.

TANG, T. & INGHAM, D. B. 1991 On steady flow past a rotating circular cylinder at Reynolds numbers 60 and 100. *Computers & Fluids* **19**, 217–230.

TASLIM, M. E., KINNEY, R. B. & PAOLINO, M. A. 1984 Analysis of two-dimensional viscous flow over cylinders in unsteady motion. *AIAA J.* **22**, 586–594.

TELIONIS, D. P. 1981 *Unsteady Viscous Flows*. Springer.

TENNANT, J. S., JOHNSON, W. S. & KROTHAPALLI, A. 1976 Rotating cylinder for circulation control on an airfoil. *J. Hydronaut.* **10**, 102–105.

TING, L. 1983 On the application of the integral invariants and decay laws of vorticity distributions. *J. Fluid Mech.* **127**, 497–506.

TOKUMARU, P. T. & DIMOTAKIS, P. E. 1991 Rotary oscillation control of a cylinder wake. *J. Fluid Mech.* **224**, 77–90.

TOWNSEND, P. 1980 A numerical simulation of Newtonian and visco-elastic flow past stationary and rotating cylinders. *J. Non-Newtonian Fluid Mech.* **6**, 219–243.

VINOKUR, M. 1983 On one-dimensional stretching functions for finite-difference calculations. *J. Comput. Phys.* **50**, 215–234.

WALOWIT, J., TSAO, S. & DIPRIMA, R. C. 1964 Stability of flow between arbitrarily spaced concentric cylindrical surfaces including the effect of a radial temperature gradient. *Trans. ASME* E: *J. Appl. Mech.* **31**, 585–593.

WAMBECQ, A. 1978 Rational Runge–Kutta methods for solving systems of ordinary differential equations. *Computing* **20**, 333–342.

WANG, C. M. & WU, J. C. 1986 Numerical solution of steady Navier–Stokes problems using integral representations. *AIAA J.* **24**, 1305–1312.

WERLÉ, H. 1984 Hydrodynamic visualization of the flow around a streamlined cylinder with suction. Cousteau-Malavard turbine sail model. *La Recherche Aérospatiale* (English Edition) **4**, 29–38.

WESTON, R. P. & LIU, C. H. 1982 Approximate boundary condition procedure for the two-dimensional numerical solution of vortex wakes. *AIAA Paper* 82-0951.

WILLIAMSON, C. H. K. 1985 Sinusoidal flow relative to circular cylinders. *J. Fluid Mech.* **155**, 141–174.

WILLIAMSON, C. H. K. 1988 The existence of two stages in the transition to three-dimensionality on a cylinder wake. *Phys. Fluids* **31**, 3165–3168.

WOOD, W. W. 1957 Boundary layers whose streamlines are closed. *J. Fluid Mech.* **2**, 77–87.

WU, J., MO, J. & VAKILI, A. 1989 On the wake of a cylinder with rotational oscillations. *AIAA Paper* 89-1024.

WU, J. C. 1975 Velocity and extraneous boundary conditions of viscous flow problems. *AIAA Paper* 75-47.

WU, J. C. 1976 Numerical boundary conditions for viscous flow problems. *AIAA J.* **14**, 1042–1049.

WU, J. C. & SAMPATH, S. 1976 A numerical study of viscous flow around an airfoil. *AIAA Paper* 76-337.

WU, J. C. & THOMPSON, J. F. 1973 Numerical solutions of time-dependent incompressible Navier–Stokes equations using an integro-differential formulation. *Computers & Fluids* **1**, 197–215.

ZANG, T. A., WONG, Y. S. & HUSSAINI, M. Y. 1982 Spectral multigrid methods for elliptic equations. *J. Comput. Phys.* **48**, 485–501.

ZEBIB, A. 1987 Stability of viscous flow past a circular cylinder. *J. Engng Maths* **21**, 155–165.

Appendix B

On the Determination of Solenoidal or Compressible Velocity Fields from Measurements of Passive or Reactive Scalars

Arne J. Pearlstein and Bonnie N. Carpenter
Department of Mechanical and Industrial Engineering
University of Illinois at Urbana-Champaign
1206 West Green Street
Urbana, IL 61801

Abstract

Recently, several techniques have been proposed for the determination of two- or three-dimensional velocity fields from measurements of one passive scalar. Here, we show that measurements of one scalar and knowledge of the equation governing its transport determine a velocity field only up to an additive vector field locally perpendicular to the gradient of the scalar field, but otherwise arbitrary. We then discuss procedures for selecting a unique velocity field from among the uncountable infinity consistent with the scalar transport data and equation. We show if that the iterative procedure of Dahm et al. (*Phys. Fluids A* 4, 2191-2206, 1992) for "solution" of a singular linear equation system (obtained using only measurements of the scalar and the equation governing its transport) does in fact converge, that outcome is, at best, an artifact of spatial discretization, and that as the resolution improves, the problem becomes increasingly ill-conditioned, becoming ill-posed in the limit of perfect resolution. We then develop a method for determining an n-dimensional (n = 2 or 3) solenoidal (divergence-free) velocity field from measurements of n − 1 passive or reactive scalars. Finally, we show how the velocity field in an n-dimensional compressible flow can be determined from measurements of density and n − 1 passive or reactive scalars.

1

I. Introduction

Determination of the velocity field in any but the simplest flows is a central problem in experimental and theoretical fluid mechanics. From an experimental standpoint, it has been possible for some time to accurately determine the time dependence of one or more velocity components at one or a small number of points, using hot-wire, hot-film, laser-Doppler (LDV), or other pointwise measurement techniques.

More recently, techniques have been developed for estimation of one or more velocity components at more than one point, using single-point methods in a scanning or flying mode (e.g., flying hot-wire[1] or scanning LDV[2]). In "scanning" mode, data is typically acquired at one point at a time along a curve $x_s(t)$. The data are thus neither full-field nor simultaneous, and are limited to one or at most two velocity components.

In the last ten years, several experimental techniques for estimating the velocity field have been developed that take advantage of essentially Lagrangian descriptions of the flow. These techniques, including particle image velocimetry (PIV) and its variants[3-4], as well as photochemical, photochromic, and luminescence methods[5,6] in which fluid elements are marked (e.g., using laser-induced photochemistry or Raman excitation of vibrational states), have in common that they attempt to follow the trajectories of either neutrally buoyant small particles or "marked" fluid elements advected by the flow, in order to infer some or all of the components of the velocity field. For the particle-based techniques, spatial resolution is limited by several factors, including the size of the particles that can be distinguished, the number of particles that can be tracked from frame to frame without ambiguity, the volume fraction and size of particles that can be added without seriously altering the flow, and the computational effort required to process the data. Other limitations of particle-based techniques have recently been discussed by Huang, Fiedler, and Wang[7,8]. For the photochemical or luminescent techniques, only a fraction of the volume of interest can be "tagged," because if all of the fluid is "marked," then none can be distinguished. For either particle or marked fluid techniques, data at any time are acquired only at the current locations of the particles or marked fluid elements. We refer to these velocity estimation techniques as being "multi-point."

2

Concurrently with development of multi-point velocimetry techniques, there has been a rapid development of optical techniques for the "full-field" determination of temperature (e.g., by means of Schlieren or liquid crystal techniques[9,10]) or concentration (dyes by absorption, other species by fluorescence or phosphorescence, e.g., laser-induced fluorescence[11]). Spatial resolution of these scalar field measurements is limited only by the resolution of the optics. This type of data is routinely acquired at high framing rates in planes by rapid scanning through a three-dimensional volume. Thus, in two dimensions it is possible to obtain simultaneous full-field scalar data, while in three dimensions, the simultaneity and full-field character of the data acquired is limited only by the scanning and framing rates. We refer to this data as being simultaneous and full-field, subject to limitations on temporal resolution imposed by framing rate, and, in three dimensions, limitations on spatial resolution in the third dimension imposed by scanning or framing rates.

Recently, techniques have been advanced[12,13] for determining velocity fields from full-field (optical) measurements of advected scalars. Such techniques have the potential to determine fully three-dimensional velocity fields with excellent spatial resolution, a key advantage over PIV-type methods, which are ultimately limited by particle size and loading constraints. In §II we show that the velocity field cannot be determined solely from measurements of a single advected scalar, and that in the published "scalar imaging velocimetry" procedure of Dahm et al.[12], the equations satisfied by the velocity field admit an infinity of solutions, each of which is indeterminate by an additive arbitrary vector field locally perpendicular to the gradient of the measured scalar field. In §III, we critically assess three techniques that have been proposed for the selection of one solution from this uncountable set. In §IV we develop a method for uniquely determining an n-dimensional (n = 2 or 3) solenoidal (divergence-free) velocity field from measurements of n − 1 passive or reactive scalars, making explicit use of the solenoidal character of the flow. In §V we show how the procedure can be extended to compressible flows for which the density field can be measured. A discussion follows in §VI.

3

II. Nonuniqueness of Velocity Fields Determined Solely from Measurement of One Scalar Field

Recently, Dahm et al.[12] have proposed that, for a conserved passive scalar ζ whose distribution evolves according to

$$\frac{\partial \zeta}{\partial t} + u \cdot \nabla \zeta = D \nabla^2 \zeta \ , \tag{1}$$

simultaneous full-field measurements of ζ suffice to determine the velocity field u. Their discussion pertains specifically to three-dimensional flows ("four-dimensional vector velocity field measurements" in the title and elsewhere refers to time as a fourth dimension). Furthermore, Dahm et al. claim that their technique does not "explicitly require $\nabla \cdot u = 0$". From that and the claim that (1) and measurements of ζ suffice to determine u, it would be logical to infer that their technique is applicable to two- or three-dimensional compressible as well as solenoidal (i.e., $\nabla \cdot u = 0$) velocity fields.

In fact, the method of Dahm et al., in which $u_{\parallel}$, the component of u parallel to the gradient of the scalar field ($\nabla \zeta$), is determined from measurements of ζ and

$$u_{\parallel} = \frac{D \nabla^2 \zeta - \partial \zeta / \partial t}{|\nabla \zeta|} \ , \tag{2}$$

and u itself is said to be determined from

$$u_{\parallel} = u \cdot \hat{e}_{\nabla \zeta} \tag{3a}$$

and

$$\nabla u_{\parallel} = u \cdot \nabla \hat{e}_{\nabla \zeta}^T + \nabla u^T \cdot \hat{e}_{\nabla \zeta} \ , \tag{3b}$$

is inherently incapable of uniquely determining the component(s) of the velocity field perpendicular to $u_{\parallel}$. To see this, we note that

$$u_G = u_{\parallel} \hat{e}_{\nabla \zeta} + h(x,t) \hat{e}_{\perp} \tag{4}$$

is a velocity field satisfying (3a), where $\hat{e}_{\perp}$ is <u>any</u> unit vector locally orthogonal to $\hat{e}_{\nabla \zeta}$ and $h(x,t)$ is an <u>arbitrary</u> scalar function of position and time. Hence, the solutions of (3a,b) are neither discrete nor countable. Furthermore, we note that (3b) can be rewritten as

$$\nabla u_{\parallel} = \nabla (u \cdot \hat{e}_{\nabla \zeta}) \ , \tag{5}$$

4

from which it is apparent that (4) satisfies (3b) also. Hence, any velocity field determined by solving (3a,b) alone (using measurements of ζ) is necessarily nonunique, because an arbitrary vector field perpendicular to $\nabla\zeta$ can be added to give a different velocity field also satisfying (3a,b). This is because the only relationship between the scalar field and the velocity field is (1), which allows no distinction to be made between velocity fields of the form (4), so long as $\hat{e}_\perp$ is locally perpendicular to the gradient of the scalar. Put another way, the component(s) (one in two dimensions and two in three dimensions) of the velocity field that play(s) no part in advecting the scalar cannot be uniquely determined solely from measurements of the scalar. This conclusion is independent of the relative diffusivities of momentum and the scalar.

Thus, it is clear that measurements of one passive scalar do not suffice to determine an arbitrary velocity field. In the context of machine vision, where in (1) ζ and u represent the image irradiance and optical flow field, respectively, and $D = 0$ (corresponding to infinite Schmidt number or Prandtl number in the present context), the inherent indeterminacy of a vector field obtained solely from measurements of the scalar field that it advects is well known[14,15], and is referred to as the aperture problem or aperture ambiguity. As discussed by Tokumaru and Dimotakis[13], one or more other "elements" (e.g., one or more additional equations, minimization of some functional, etc.) is required in order to render u unique. As discussed below, we note that the nature of the additional element(s) used to select a unique u determines how well the selected u corresponds to the actual velocity field.

Alternatively, the claim[12] that (3b) has a unique solution for u because (3b) constitutes three linear equations in three unknowns is easily seen to be false since the right-hand side of (3b) is identical to the right-hand side of (5), from which it is easily seen that (4) satisfies (5) (and hence 3b) for any $h(x, t)$ so long as the vector field $\hat{e}_\perp$ is locally perpendicular to $\nabla\zeta$.

III. Selecting a Unique Velocity Field

The real issue then, as recognized by Tokumaru and Dimotakis[13], is how one goes about selecting the correct u from among the uncountable infinity consistent with the scalar transport data and equation. Clearly, any technique that sufficiently constrains the velocity field will select a unique u. Thus, rendering

5

u unique is not equivalent to selecting the correct u. In the following subsections, we discuss three procedures that accomplish, or claim to accomplish, the selection of a unique u.

III.A. The "Iterative Inversion" Approach

Dahm et al. have claimed[12] that "solution" of (3b) by a particular iterative technique selects the correct u (i.e., the velocity field that satisfies conservation of mass) from the infinity of other solutions of (3a) and (3b). Specifically, in reference 12, (3b) is discretized and written as

$$b = A_1 v^{(m)} + A_2 v^{(m-1)} \qquad (6)$$

at each time, where each element of the vector b is an approximation to a component on the left-hand side of (3b) at a point for which scalar data are available, the two terms on the right-hand side are discretizations of the corresponding terms on the right-hand side of (3b), and v is a vector of unknown velocity components at the discrete points. It was originally claimed[12] that "Successive iterations based on Eq. (7)* can be made until the velocity field $u^{(k)}$ converges to a self-consistent result". In addition the authors claim that "Stable, rapid, and accurate convergence is achieved". The correctness of the computed velocity field was attributed to the smallness of the second term in (6), from which it was said to follow that the initial iterate ($v^{(0)} = A_1^{-1} b$) was necessarily close to the correct solution of (3a,b).

In fact, from the indeterminacy of the solutions of the continuous problem (3a,b), it follows that for a faithful discretization

$$b = Av \qquad (7)$$

of (3b), the matrix $A = A_1 + A_2$ is either singular (exactly or numerically; the latter situation gives an ill-conditioned linear equation system, so the two possibilities are in practice equivalent) at any spatial resolution, or is singular in the limit of infinite resolution, in which case the method necessarily breaks down as the spatial resolution of the data improves indefinitely. Here we show that any claim that the iteration (6) "converges" is inconsistent with the singularity of A. For general A, it can be verified by direct substitution that the solution of

---

* equivalent to our (6)

6

$$b = A_1 v^{(m)} + (A - A_1) v^{(m-1)} \tag{8}$$

is

$$v^{(k)} = A_1^{-1} \sum_{j=0}^{k-1} \left[I - A A_1^{-1} \right]^j b \ . \tag{9}$$

Since

$$\sum_{j=0}^{\infty} B^j = (I - B)^{-1} \tag{10}$$

if the infinite sum exists, we see that $\det(AA_1^{-1}) \neq 0$ is a necessary condition for the existence of a "converged" formal solution

$$v = \lim_{k \to \infty} A_1^{-1} \sum_{j=0}^{k-1} \left[I - A A_1^{-1} \right]^j b = A_1^{-1} \left[I - (I - A A_1^{-1}) \right]^{-1} b = A_1^{-1} (A A_1^{-1})^{-1} b \ . \tag{11}$$

of (8). But A is singular, so no "converged" solution of (8) exists, no matter how A is decomposed. Thus, the meanings of the convergence claims made by Dahm et al.[12] are not clear. With regard to the statement[12] that "The ultimate level of improvement attainable through further iterations is, of course, limited by numerical processing errors introduced by the discrete implementation of Eq. (7)", we note that in the limit of infinite resolution and no noise, the matrix A is exactly singular, and the method necessarily fails. If in fact "converged" results are produced at all, that would simply be an artifact of the discretization. Moreover, since no solution of the continuous problem can be obtained by the iterative method described, any "solution" of the discrete problem obtained by this technique should be expected to depend sensitively on both noise in the data and the details of the discretization.

III.B. The "Variational" Approach

More recently, it has been claimed that in three dimensions u can be determined from measurement of a single scalar if one minimizes the positive semidefinite integral

$$E = \iiint_V \left\{ \left[\frac{\partial \zeta}{\partial t} + u \cdot \nabla \zeta - D \nabla^2 \zeta \right]^2 + \phi (\nabla \cdot u)^2 + \lambda (\nabla u : \nabla u)^j \right\} dV \ , \tag{12}$$

where the value of the exponent j is variously given as 1 or 2, and ϕ and λ are constant weighting factors. This is an example of how an additional "element" can be used to select a unique u.

7

It is clear that for $\lambda = 0$, minimization of (12) is mathematically equivalent to satisfying (1) and $\nabla \cdot u = 0$. In the following section, it is shown that this approach is correct for two-dimensional solenoidal flows. For three-dimensional flows, (1) and $\nabla \cdot u = 0$ are insufficient to uniquely determine u. On the other hand, for $\lambda \neq 0$, one must hope that minimization of (12) results in both satisfaction of (1) and $\nabla \cdot u = 0$, as well as in minimization of the viscous dissipation. It has been claimed that the viscous dissipation achieves a minimum in physically realized flows, and that minimization of E selects the correct u.

In fact, the class of flows for which it can be shown that the viscous dissipation is minimized (compared to all other kinematically admissible flows satisfying the same boundary conditions) is small and rather uninteresting. It consists of those flows for which either

a) the flow is steady and the inertial terms vanish identically (Helmholtz[16]), or

b) the viscous terms are derivable from a single-valued scalar potential (Rayleigh[17]).

Furthermore, for sufficiently large λ, it is likely that minimization of E will drive the dissipation to zero at the expense of satisfying (1) and $\nabla \cdot u = 0$.

It is clear that minimization of (12) cannot be expected to yield a correct u for compressible flow.

Neither condition a) nor b) obtains in the flows to which the method has been applied.

III.C. The "Smoothness" Approach

Tokumaru and Dimotakis[13] have recently developed an essentially Lagrangian technique that considers situations for which

$$\frac{D(t_1-t_0)}{\ell^2} \ll 1 , \tag{13}$$

where ℓ is the imaging resolution, and t_1-t_0 is the time interval between consecutive images of the scalar field. They integrate (1) (with the diffusive term set to zero) to get

$$\zeta[\xi(x,t_1)] - \zeta[\xi(x,t_0)] = 0 , \tag{14}$$

where the displacement field is denoted by $\xi(x,t)$, and the initial locations of the fluid elements are given by $\xi(x,t_0) = x$.

Tokumaru and Dimotakis render the velocity field unique by minimizing the integral (over the measurement volume) of the sum of the squares of the left-hand side of (14) from zero, and a measure of smoothness of the displacement field $\xi(x,t)$ and its spatial derivatives. This method requires solution of a global linear equation system at each time in order to find a unique displacement field that minimizes the error in (14) while maintaining its own smoothness. Since there is no physical requirement that the "smoothest" velocity field be the correct one in any particular flow, one cannot *a priori* assume that this technique yields the correct u. However, as pointed out by Hildreth[18] in the machine vision context, although the "velocity field of least variation is, in general, not the physically correct one", it is often qualitatively similar. Tokumaru and Dimotakis[13] have applied their method to experimental data from several carefully chosen flows in which they have created and imaged appropriate scalar distributions. Their results for steady circular Couette flow (with a time-dependent scalar field) are excellent, while those obtained using single two-dimensional slices of the three-dimensional transitional flow past a circular cylinder are qualitatively reasonable.

IV. Unique Determination of n-dimensional Solenoidal Velocity Fields from Measurements of n–1 Scalar Fields

In this section, we describe a technique employing full-field measurements of $n-1$ scalars to determine solenoidal (divergence-free, or "incompressible") n-dimensional velocity fields. Our objective is to develop a method that is "consistent", by which we mean two things. First, the method should extract the correct velocity field when there is sufficient scalar data to do so. Second, the error in the extracted velocity field should go to zero as the spatial and temporal resolution of the scalar measurements improve. In general, these requirements dictate that the additional "element" used to render u unique be satisfied exactly in the flow, and not implicit in the scalar transport equation. For two-dimensional flows, we show that measurement of one scalar (temperature or concentration) suffices to uniquely determine a solenoidal velocity field, whereas for three-dimensional flows, measurements of two scalars (temperature and concentration or two independent concentrations) having nonparallel gradients are required. Our technique is in principle applicable to steady or unsteady, laminar or turbulent, two- or three-dimensional

9

flows. Key features are that no velocity components need be measured, the number of measured scalars required is one less than the spatial dimensionality, and the method should give a velocity field that faithfully approximates the correct **u** as the spatial or temporal resolution of the scalar measurements improves. The computations are local in a sense made more precise below, and do not require solution of a large linear (or nonlinear) equation system. For steady or time-periodic three-dimensional flows, the two scalars need not be measured simultaneously.

Our technique is based on the recognition that if the transport equation(s) for the scalar(s) is (are) linear in the velocity components, then it (they) and the so-called incompressible continuity equation

$$\nabla \cdot \mathbf{u} = 0, \tag{15}$$

constitute two (three) linear equations in two (three) velocity components.

Our analysis will be presented in a Cartesian coordinate system. (Results for general curvilinear coordinate systems will be presented in §IV for the compressible case.) In two dimensions, we present the development in terms of an equation for transport of a single species (the concentration of which is denoted by C) in a binary fluid. We allow for that species to react, with kinetics that are essentially arbitrary so long as they are known and the rate of reaction depends solely on C. (In the development of the three-dimensional analysis, we show how temperature-dependent kinetics can be accommodated.) Under a broad range of conditions, the scalar equation for transport of C can be approximated by

$$\frac{\partial C}{\partial t} + \mathbf{u} \cdot \nabla C = D\nabla^2 C + R(C), \tag{16}$$

where D is the binary diffusion coefficient and ∇^2 is the two-dimensional Cartesian Laplacian. If temperature is the passive scalar for which full-field measurements are available, then (16) will be replaced by an energy equation, identical to (16) if D is replaced by κ and the reaction rate R(C) is set to zero. In two dimensions, (16) can be written as

$$\frac{\partial C}{\partial t} + u\frac{\partial C}{\partial x} + v\frac{\partial C}{\partial y} = D\nabla^2 C + R(C), \tag{17}$$

which together with the two-dimensional form

10

$$\frac{\partial u}{\partial x} + \frac{\partial v}{\partial y} = 0, \tag{18}$$

of (15) constitute a pair of linear equations in u(x,y,t) and v(x,y,t). Solving (17) for v and substituting into (18) yields

$$\left\{ \nabla C \times \nabla \left[\frac{u}{\partial C/\partial y} \right] \right\} \cdot e_z = \frac{\partial}{\partial y} \left[\frac{G}{\partial C/\partial y} \right], \tag{19a}$$

while solution of (17) for u and substitution into (18) yields

$$\left\{ \nabla C \times \nabla \left[\frac{v}{\partial C/\partial x} \right] \right\} \cdot e_z = -\frac{\partial}{\partial x} \left[\frac{G}{\partial C/\partial x} \right], \tag{21b}$$

where

$$G = D\nabla^2 C - \frac{\partial C}{\partial t} + R(C). \tag{20}$$

Equations (19a) and (19b) are two linear, first-order, uncoupled equations for u and v.

In three dimensions we consider two scalars, at least one of which is a concentration variable. The second scalar can be either temperature or another concentration. In what follows, we will take the second scalar to be temperature, and assume that the thermal properties are temperature-independent and that the viscous dissipation heating term in the energy equation can be neglected. Only trivial changes in the discussion are required if both scalars are concentrations. In (16), ∇^2 is now the full three-dimensional Laplacian. The two transport equations are then

$$\frac{\partial C}{\partial t} + u\frac{\partial C}{\partial x} + v\frac{\partial C}{\partial y} + w\frac{\partial C}{\partial z} = D\nabla^2 C + R(T,C), \tag{21a}$$

and

$$\frac{\partial T}{\partial t} + u\frac{\partial T}{\partial x} + v\frac{\partial T}{\partial y} + w\frac{\partial T}{\partial z} = \kappa\nabla^2 T + \frac{(-\Delta H)}{\rho c_p} R(T,C), \tag{21b}$$

which together with the three-dimensional version

$$\frac{\partial u}{\partial x} + \frac{\partial v}{\partial y} + \frac{\partial w}{\partial z} = 0, \tag{22}$$

11

of (15) constitute three linear equations for u, v, and w. We note that any kinetic scheme (including one with temperature-dependent rates) can be accommodated, so long as the rate expression is a known expression of the form $R(T,C)$.

Three linear, first-order equations

$$(\nabla C \times \nabla T) \cdot \nabla(u/\alpha) = \left[\nabla T \times \nabla(H_2/\alpha) - \nabla C \times \nabla(H_1/\alpha) \right] \cdot e_x \tag{23a}$$

$$(\nabla C \times \nabla T) \cdot \nabla(v/\gamma) = \left[\nabla T \times \nabla(H_2/\gamma) - \nabla C \times \nabla(H_1/\gamma) \right] \cdot e_y \tag{23b}$$

$$(\nabla C \times \nabla T) \cdot \nabla(w/\delta) = \left[\nabla T \times \nabla(H_2/\delta) - \nabla C \times \nabla(H_1/\delta) \right] \cdot e_z \tag{23c}$$

analogous to (19a) and (19b) can be derived from (21a,b) and (22), where

$$H_1 = D\nabla^2 C - \frac{\partial C}{\partial t} + R(T,C) , \tag{24a}$$

$$H_2 = \kappa\nabla^2 T - \frac{\partial T}{\partial t} + \frac{(-\Delta H)}{\rho c_p} R(T,C), \tag{24b}$$

and

$$\alpha = \frac{\partial C}{\partial y}\frac{\partial T}{\partial z} - \frac{\partial C}{\partial z}\frac{\partial T}{\partial y}, \tag{25a}$$

and

$$\gamma = \frac{\partial C}{\partial z}\frac{\partial T}{\partial x} - \frac{\partial C}{\partial x}\frac{\partial T}{\partial z}, \tag{25b}$$

and

$$\delta = \frac{\partial C}{\partial x}\frac{\partial T}{\partial y} - \frac{\partial C}{\partial y}\frac{\partial T}{\partial x} \tag{25c}$$

are the components of $\nabla C \times \nabla T$.

Equations (19a,b) or (23a-c) constitute systems of linear first-order uncoupled hyperbolic equations in the velocity components u and v, and u, v, and w, respectively. Given the scalar field data, the solution of these equation systems is made unique by specification of appropriate boundary conditions. (As the unknowns are components of the velocity, the required boundary conditions will involve velocity

components, rather than the transported scalars.) Equations (19a,b) or (23a-c) can then be integrated along characteristics. We note that in two dimensions, the characteristics are the same for (19a,b), and that in three dimensions, the characteristics are the same for (23a-c). We note that no time derivatives of the velocity components appear in (19a,b) or (23a-c), so that no initial data on the velocity field are required. A desirable consequence of the fact that (19a,b) and (23a-c) are not initial value problems is that errors in the determination of the velocity field do not grow temporally.

In two dimensions, it is clear that at any point at which either component of the gradient of the scalar vanishes, (19a) or (19b) will have a singularity. In three dimensions, equations (23a), (23b), or (23c) will be singular at points where α, γ, or δ vanish. From the standpoint of extracting velocity fields from experimental scalar data, and more importantly, in order to wisely select boundary conditions, diffusivity ratios, and other factors that affect the scalar field(s) from which the velocity field is to be extracted, it is important to understand the nature of the singularities, and to develop techniques for dealing with them, if possible.

First, we classify the singularities of (19a,b) and (23a-c). We first consider the two-dimensional case. If exactly one component of the scalar gradient vanishes, then one component of u can be determined from (19a) or (19b), and the other can be found from (18). For example, if $\partial C/\partial x = 0$, then (19a) can be used to find u and (17) can be used to determine v from

$$v = \frac{D\nabla^2 C - \partial C/\partial t}{\partial C/\partial y} \ . \tag{26}$$

In practice, it is advantageous to integrate (19a) and compute v from (26), and to compare the values of u and v at each point along the common characteristic to the values obtained by integrating (19b) and using

$$u = \frac{D\nabla^2 C - \partial C/\partial t}{\partial C/\partial x} \ . \tag{27}$$

Thus, when one gets close to a curve on which $\partial C/\partial x = 0$ for example, the results of the above two procedures will begin to differ, and one can use the results obtained from (19b) and (26). That the scalar field and solenoidal constraint still provide enough information to determine u in this case is easily seen,

since the general case can be rewritten in terms of local coordinates parallel and perpendicular to ∇C, characterized by unit vectors $\hat{e}_{\nabla\zeta}$ and $\hat{e}_\perp$, such that the component of ∇C in the direction of $\hat{e}_\perp$ is zero.

When ∇C vanishes, it might seem from (17) that the scalar field provides no information about u. This is indeed true if ∇C vanishes identically in some area, in which case there is insufficient information to determine u in the interior of that area. If, on the other hand, ∇C vanishes either at an isolated point (corresponding to the intersection of the curves along which $\partial C/\partial x = 0$ and $\partial C/\partial y = 0$) or along a curve, then we can in fact determine u. In two dimensions, we begin by using index notation to rewrite (17) as

$$u_j \frac{\partial C}{\partial x_j} = G \qquad\qquad i = 1,2 . \qquad\qquad (28)$$

Taking the gradient of both sides of (28), we obtain

$$u_j \frac{\partial^2 C}{\partial x_i x_j} = \frac{\partial G}{\partial x_i} \qquad\qquad i = 1,2 . \qquad\qquad (29)$$

when the gradient of C vanishes. Thus, we have two (linearly independent) nonhomogeneous equations for the components of u. We find that

$$u = \frac{G_x C_{yy} - G_y C_{xy}}{C_{xx} C_{yy} - C_{xy}^2} \qquad\qquad v = \frac{G_y C_{xx} - G_x C_{xy}}{C_{xx} C_{yy} - C_{xy}^2} . \qquad (30a,b)$$

We note that (30a,b) can be obtained from (17) only if $\nabla C = 0$. That the solenoidal constraint is not required in order to specify the velocity field in this case is due to the fact that another constraint, namely $\nabla C = 0$, obtains.

Thus, we see that unless ∇C vanishes identically over an area, "singularities" in (19a,b) are "removable" in the sense that the velocity field can be uniquely determined at points or along curves where one or both components of ∇C vanish.

In three dimensions, $\nabla C \times \nabla T$ plays the part of ∇C, and the vanishing of one or two components of the cross product of the gradients of the scalars corresponds to a change to a local coordinate system

14

with unit vectors parallel and tangential to the cross product. In that case, formulas analogous to (26) and (27) can be derived for the components of **u**. If all three components of $\nabla C \times \nabla T$ vanish (i.e., the gradients of C and T are parallel) in a volume, then the scalar transport equations and the solenoidal constraint provide insufficient information for determination of **u** in that volume. In the event that $\nabla C \times \nabla T$ vanishes on a curve or on a surface, expressions for u, v, and w analogous to (30a,b) for the two-dimensional case can be derived. The apparent singularity in (23a-c) is completely removable unless $\nabla C \times \nabla T$ vanishes in a volume.

Finally, we note that one can easily show that characteristics originating on a boundary will emanate into the flow (as opposed to remaining on the boundary) if the normal component of the scalar gradient (in two dimensions) or the normal component of the cross product of the scalar gradients (in three dimensions) is nonzero. In two dimensions, this point argues strongly for use of temperature as the scalar, since most walls are impermeable to most species (i.e., $\mathbf{n} \bullet \nabla C = 0$). In three dimensions, a nonisothermal wall through which the second scalar does not penetrate will be consistent with $\mathbf{n} \bullet (\nabla C \times \nabla T) \neq 0$.

V. Unique Determination of n-dimensional Compressible Velocity Fields from Measurements of Density and n–1 Other Scalar Fields

In this section, we show how the approach of §III can be extended to deal with the case in which the equation for conservation of mass is

$$\frac{\partial \rho}{\partial t} + \mathbf{u} \bullet \nabla \rho + \rho \nabla \bullet \mathbf{u} = 0 \ . \tag{31}$$

We again use

$$\frac{\partial C}{\partial t} + \mathbf{u} \bullet \nabla C = D\nabla^2 C + R(T,C) \tag{32a}$$

and

$$\rho c_v \left(\frac{\partial T}{\partial t} + \mathbf{u} \bullet \nabla T \right) = \nabla \bullet k\nabla T + \frac{c_p - c_v}{\beta} \left(\frac{\partial \rho}{\partial t} + \mathbf{u} \bullet \nabla \rho \right) + (-\Delta H)R(T,C) \ , \tag{32b}$$

15

where β is the thermal expansion coefficient, to eliminate two components of u before substituting into the continuity equation [this time (31)] to get a hyperbolic equation for the third component. Doing this three times, we get, in general curvilinear coordinates,

$$L \cdot \nabla\left(\frac{f\rho u_i}{h_i L_i}\right) = -f\frac{\partial\rho}{\partial t} + \left[\nabla T \times \nabla\left(\frac{f\rho H_3}{L_i}\right) - \nabla C \times \nabla\left(\frac{f\rho H_1}{L_i}\right)\right] \cdot e_i \qquad (33)$$

where $L = \nabla C \times (\nabla T + \Gamma\nabla\rho)$, $\Gamma = (1 - c_p/c_v)/(\beta\rho)$, h_1, h_2, and h_3 are metric coefficients, $f = h_1 h_2 h_3$, H_1 is as defined in §III, and

$$H_3 = \frac{\nabla \cdot k\nabla T}{\rho c_p} - \frac{\partial T}{\partial t} + \frac{(-\Delta H)}{\rho c_p}R(T,C) \quad . \qquad (34)$$

In the compressible case, singularity corresponds to the vanishing of components of L, and the approach is similar to that described in §III.

For a constant density fluid, $c_p = c_v$, and we recover the solenoidal results given in §III.

VI. Discussion

Determination of an n-dimensional velocity field (n = 2 or 3) requires n "elements," each constituting an independent constraint on the velocity components. In our approach, for a two-dimensional solenoidal velocity field these are equations (17) and (18), where the derivatives of the scalar field in (17) are obtained from experiment. In three dimensions, we take the three elements to be equations (21a,b) and (22), where the scalar fields and their derivatives are obtained from experiment. For compressible flow, one can use the continuity equation (31) and $n-1$ of equations (32a) and (20b), where the density and advected scalar(s) are obtained from experiment.

We note that, for solenoidal u, one modification of the approach presented above might be to employ the same elements to compute one velocity component using the corresponding hyperbolic equation, and to use the $n-1$ transport equations (17, or 21a,b), which are linear and algebraic in the other components, to determine the remainder of the velocity field.

A rather different set of n elements might be full-field measurements of $n-r$ velocity components, $r-1$ transport equations, and a continuity equation.

In any case, the fact that n independent equations are required to determine n unknowns means that a single transport equation along with measurement of the corresponding scalar field does not uniquely determine a solenoidal velocity field in three dimensions, or a compressible velocity field in two dimensions, let alone a compressible velocity field in three dimensions.

We note that the feasibility of our technique will depend in large part on one's ability to create scalar distributions for which ∇C (in two dimensions) or $\nabla C \times \nabla T$ (in three dimensions) is not only not zero everywhere in the interior of an area (in two dimensions) or a volume (in three dimensions), but is also not small (compared to the measurement sensitivity divided by the spatial resolution) in the interior of a volume or area. This will, in general, require some care to be exercised in setting up the scalar field(s). In addition to the choice of boundary conditions for the scalar, and some limited flexibility in the choice of diffusivities, one may also want to take advantage of the fact that, since the technique is applicable to scalars whose transport is described by (16) in two dimensions and (19a,b) in three dimensions, one can consider various "volumetric" methods for influencing the scalar fields, in which R(C) or R(T,C) is replaced or augmented by a spatially nonuniform "source term".

Finally, we note that our technique is an ideal candidate for parallelization. The integration along characteristics uses only local information along the characteristic, and does not involve solution of a "global" equation system, as is required by the "iterative inversion" and "variational" approaches. Moreover, integration along the characteristics is a process that can be parceled out on the basis of one processor per characteristic. The fact that no large linear equation system need be solved (the "variational technique" described in §II.B. involves a linear equation system so large as to require iterative solution), makes the process eminently suitable for real-time use.

Acknowledgments

17

References

1. D. Coles and A.J. Wadcock, "Flying-hot-wire study of flow past an NACA 4412 airfoil at maximum lift," *AIAA J.* **17**, 321-329 (1979).

2. D.R. Williams and M. Economou, "Scanning laser anemometer measurements of a forced cylinder wake, "*Phys. Fluids*, **30**, 2283-2285 (1987).

3. R.J. Adrian, "Particle imaging techniques for experimental fluid mechanics, "*Ann. Rev. Fluid Mech.* **23**, 261-304 (1991).

4. C.E. Willert and M. Gharib, "Digital particle image velocimetry", *Expts. in Fluids*, **10**, 181-193 (1991).

5. R.E. Falco and C.C. Chu, "Measurement of two-dimensional fluid dynamic quantities using a photochromic grid tracing technique ,"*SPIE J.* **814**, 706-710 (1987).

6. R. B. Miles, D. Zhou, B. Zhang, W.R. Lempert, and Z.-S. She, "Fundamental turbulence measurements by Relief flow tagging", *AIAA J.* **31**, 447-458 (1993).

7. H.T. Huang, H.E. Fiedler, and J.J. Wang, "Limitation and improvement of PIV, Part I: Limitation of conventional techniques due to deformation of particle image patterns", *Expts. in Fluids*, **15**, 168-174 (1993).

8. H.T. Huang, H.E. Fiedler, and J.J. Wang, "Limitation and improvement of PIV, Part II: Particle image distortion, a novel technique", *Expts. in Fluids*, **15**, 1263-273 (1993).

9. R.J. Goldstein, "Optical systems for flow measurement: shadowgraph, Schlieren, and interferometric techniques", pp. 377-422 in "Fluid Mechanics Measurements," ed. R.J. Goldstein, Hemisphere, New York (1983).

10. H.S. Rhee, J.R. Koseff, and R.L. Street, "Flow visualization of a recirculating flow by rheoscopic liquid and liquid crystal techniques," *Expts. in Fluids*, **2**, 57-64 (1984).

11. P.H. Paul and N.T. Clemens, "Subresolution measurements of unmixed fluid using electronic quenching of NO $A^2\Sigma^+$," *Optics Letters*, **18**, 161-163 (1993).

12. W.J.A. Dahm, L.K. Su, and K.B. Southerland, "A scalar imaging velocimetry technique for fully resolved four-dimensional vector velocity field measurements in turbulent flows," *Phys. Fluids A* **4**, 2191-2206 (1992).

13. P.T. Tokumaru and P.E. Dimotakis, "Image correlation velocimetry", *Expts. in Fluids*, accepted for publication.

14. D.W. Murray and B.F. Buxton, "Experiments in the Machine Interpretation of Visual Motion," MIT Press, Cambridge (1990).

15. A. Singh, "Optics Flow Computation: A Unified Perspective," IEEE Computer Society Press, Los Alamitos (1991).

16. Helmholtz, H., "Zur Theorie der stationären ströme in reibenden Flüssigkeiten", *Verhandlungen des naturhistorisch-medicinischen Vereins zu Heidelberg* **V**, 1-7 (1868). [Also in "Wissenschaftlichte Abhandlungen von Hermann Helmholtz," I, 223-230, J.A. Barth, Leipzig (1882).]

17. Rayleigh, Lord, "On the motion of a viscous fluid", *Phil. Mag.* [6] **26**, 776-786 (1913).

18. E.C. Hildreth, "The Measurement of Visual Motion," MIT Press, Cambridge (1984).